LBL-5479
c.1

INFLUENCE OF POROSITY ON THE MECHANICAL PROPERTIES OF LEAD ZIRCONATE-TITANATE CERAMICS

Dipak Ranjan Biswas
(Ph. D. thesis)

September 1976

Prepared for the U. S. Energy Research and
Development Administration under Contract W-7405-ENG-48

LBL-5479
c.1

INFLUENCE OF POROSITY ON THE MECHANICAL PROPERTIES OF LEAD ZIRCONATE-TITANATE CERAMICS

Table of Contents

Note: pages 47-48 of the document are not available.

Report Coordination

08-30-2010

INFLUENCE OF POROSITY ON THE MECHANICAL PROPERTIES OF LEAD ZIRCONATE-TITANATE CERAMICS

Dipak Ranjan Biswas

Materials and Molecular Research Division, Lawrence Berkeley Laboratory
and Department of Materials Science and Engineering,
University of California, Berkeley, California 94720

ABSTRACT

Niobium doped lead zirconate-titanate (PNZT) was used to investigate the effect of porosity on the mechanical properties of a polycrystalline ceramic. Spherical and acicular pores (25-150μm) were introduced by using organic materials and the grain size (2-5μm) was constant throughout the study. The very fine pores (2-3μm) were formed by varying the sintering conditions and the grain size was comparable to the pore size. The fracture strength of the ceramic was measured by simple 4-point bending. A sonic resonance technique was used to measure the elastic modulus and the double torsion method was used to measure the fracture toughness of the ceramic. The effect of porosity on the fracture strength was predicted quite well by Weibull's probabilistic approach. The elastic modulus showed a linear relationship with increase in porosity (110-150 μm) and showed a higher value for PNZT-fine pore (2-3μm) ceramics at same volume percent porosity. A decrease in fracture toughness with increase in porosity (110-150μm) was also observed. It has been found that the fine pores in PNZT polycrystalline ceramic gave higher strength, elastic modulus and fracture toughness compared to the PNZT - large pore ceramics at equivalent porosities. Fracture surface analysis by scanning electron microscopy showed that the fracture origin was at the tensile surface, at the edges of the specimen and just underneath the tensile surface.

I. INTRODUCTION

The microstructures of polycrystalline ceramic materials are usually characterized by the grain size, porosity, and presence of secondary phases. Mechanical properties of ceramics are intimately related to their microstructure. Most polycrystalline ceramic materials have some porosity. This porosity reduces the mechanical strength considerably and is extremely important where ceramics are used as structural materials. During the past 20 years, a number of studies have been performed to elucidate the effect of porosity on strength[1-8] and elastic modulus.[7] General relationships are beginning to emerge. Most of these investigations considered only the total porosity and neglected the size and shape of the pores. Therefore, an attempt has been made to perform a systematic study of the mechanical properties of a well characterized polycrystalline ceramic containing a controlled amount of porosity with variations in the volume of pores, pore size and pore shape. Because of the extensive work on processing of lead zirconate-titanate ceramics in this laboratory, it was selected as the material for study. The fabricated samples were fine grained (2-5μm) ceramics in which the grain growth during processing was controlled by doping with one mole percent niobium oxide (PNZT). The advantage of using this material was that specimens were easy to fabricate with good reproducibility and control of grain size from batch to batch. It was found that the addition of a small amount of excess PbO enhances the ease of fabricating this material by sintering and densities over 99% of the theoretical value could be obtained without difficulty. Spherical and acicular pores were introduced into the specimens using organic materials mixed with PNZT powders prior to processing and sintering.

Four point bend strength, elastic modulus and fracture toughness were determined at room temperature on samples with controlled microstructures. Microstructures and fractographic analysis were done by scanning electron microscopy.

II. POROSITY AND MECHANICAL PROPERTY RELATIONS

A. Porosity and Strength

The strength of polycrystalline brittle materials is extremely sensitive to porosity. Balshin[1] determined from experimental studies that the strength of porous brittle polycrystalline materials varies with porosity as,

$$\sigma = \sigma_o (1-P)^m \tag{1}$$

where σ is the strength of porous material, σ_o is the strength of the non-porous material, P is the fractional volume porosity and m is an emperical constant. Ryshkewitch[2] determined the compressive strength of porous Al_2O_3 and magnesia stabilized ZrO_2. Duckworth[3] showed that Ryshkewitch's data followed a relationship described by the equation,

$$\sigma = \sigma_o \exp^{-bP} \tag{2}$$

where b is an empirical constant. Again for porous polycrystalline Al_2O_3, Coble and Kingery[4] fitted their results to an equation of the form,

$$0.6P = \exp - [\sigma/8000(1-P)] \tag{3}$$

Subsequently Knudsen[5] concluded that equation (2) gave better agreement with his experimental results on ThO_2. Knudsen also pointed out that the relationship between strength, porosity and grain size would fit an expression,

$$\sigma = KG^{-a} \exp^{-bP} \tag{4}$$

where G is the grain size and a, b, and K are constants. Passmore et al.[6] concluded from studies on polycrystalline Al_2O_3 that an equation to best describe their experimental results was of the form

$$\sigma = KG^{-a+cP} \exp^{-bP} \qquad (5)$$

where K, a, b, and c are constants. Bailey and Hill[7] noted variations in b between 4 and 11 in various oxide ceramics but values as low as 1 and as high as 30 have been reported. The significance of b is not well understood since relation (2) is empirical.

Carniglia[8] developed a model for the effect of porosity on the strength of ceramics. He used experimental data from the literature for polycrystalline Al_2O_3 and a borosilicate glass to test his model. For polycrystalline ceramics the expression for the mean strength was

$$\log \bar{\sigma} = \log\left[\left(\sigma_\infty + \sigma_1 G^{-1/2}\right) F(P)\right] \qquad (6)$$

where G is the mean grain size. σ_∞ and σ_1 are constants and F(P) was given by

$$\log F(P) = -\left[\frac{\alpha P}{4.606} - 1/2 \log \frac{1}{1-P}\right] - S \log\left[\frac{\frac{1}{P^{1/3}} - \frac{11}{16} - \frac{P^{2/3}}{8} - \frac{3P^{4/3}}{16}}{\frac{1}{P^{1/3}} - 1}\right].$$

The quantity in the first bracket (the load bearing area function) applied to polycrystals containing intra-granular porosity and the quantity in the second bracket applied to cases where failure initiating flaws are very small compared to interpore distance. The constant, α [from $E_p/E_o = \exp(-\alpha P)$ where E_p is the Young's modulus of porous body and E_o is the Young's modulus of solid matrix], was determined experimentally. The pore shape factor, S, was greater than one depending upon the degree of asymmetry of intergranular porosity.

The exponential relationship of Young's modulus with porosity is not always true for many ceramic systems. For a given system it is necessary to ascertain if very localized stress concentrations play a dominant role in determining the strength or whether it is the reduction in cross-sectional area due to pores or a combination of both that is important.

The effect of stress concentrations on the average strength of brittle solids, subjected to tensile states of stress, is invariably less than would be expected from the "theoretical" elastic stress concentration factor. This observation can be explained qualitatively by noting that brittle solids contain a distribution of inherent flaws of varying severity. The probability of finding the most severe flaw in the specimen in the localized stress field caused by a pore is low. For this reason, the flaws responsible for fracture with stress concentrations present will be less severe, generally, than those in smooth specimens where large regions are exposed to uniform stresses.

A quantitative explanation of the effect of stress concentrations on strength of brittle materials is possible in some cases by using the Weibull[9] probabalistic treatment. The assumptions involved in applying the Weibull treatment to multiaxial stresses and details of the formulation are given by Vardar and Finnie.[10] Finnie and Vardar[11] considered the state of stress around a pore for a porous specimen as shown in Fig. 1 in which a specimen of total volume V is loaded by a nominal stress S. The specimen contains N spherical pores, each of volume V_o. They assumed that the pores are far enough apart so that the regions of high stress concentrations do not interact. Taking the highly stressed region around a pore to have a volume V_1, which will be specified later, the remaining material of volume V_2 is assumed to be subjected only to

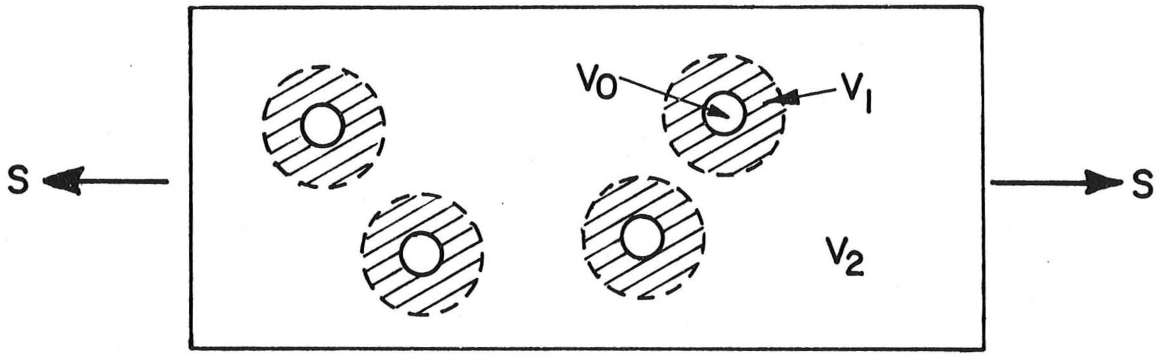

XBL 7512-9460

Fig. 1. Specimen of total volume V containing N spherical pores and subjected to uniaxial tensile stress S.

uniaxial stress.

$$\text{Hence, } V = V_2 + NV_o + NV_1 \tag{7}$$

For an isolated spherical hole, as shown in Fig. 1, the stress state for elastic behavior was given by Goodier.[12]

Using the coordinate system shown in Fig. 2, the stresses are,

$$\sigma_r = \frac{S}{2}(1 - \cos 2\theta) + \frac{S}{2(7-5\nu)}\left(\frac{a}{r}\right)^3 \left\{(5\nu-13) + 6\left(\frac{a}{r}\right)^2 + \left[5(5-\nu) - 18\left(\frac{a}{r}\right)^2\right]\cos 2\theta\right\} \tag{8}$$

$$\sigma_\theta = \frac{S}{2}(1 + \cos 2\theta) + \frac{S}{4(7-5\nu)}\left(\frac{a}{r}\right)^3 \left\{(13-20\nu) - 3\left(\frac{a}{r}\right)^2 - \left[5(1-2\nu) - 21\left(\frac{a}{r}\right)^2\right]\cos 2\theta\right\} \tag{9}$$

$$\sigma_\alpha = \frac{3\,S}{4(7-5\nu)}\left(\frac{a}{r}\right)^3 \left\{1 - 3\left(\frac{a}{r}\right)^2 - 5\left[(1-2\nu) - \left(\frac{a}{r}\right)^2\right]\cos 2\theta\right\} \tag{10}$$

$$\tau_{r\theta} = \frac{S}{2(7-5\nu)}\left(\frac{a}{r}\right)^3 \left[-5(1+\nu) + 12\left(\frac{a}{r}\right)^2\right]\sin 2\theta - \frac{S}{2}\sin 2\theta \tag{11}$$

The ratios of the stress components, or of the principal stresses σ_1, σ_2, σ_3, to the nominal stress S are functions only of r/a and θ for a given Poisson's ratio, ν. The maximum stress concentration $\sigma_\theta(r = a, \theta = 0) \div S$ is $(27-15\nu) / (14-10\nu)$. For a range of Poisson's ratio S varies from a value of 2 for $\nu = 0.2$ to 2.045 for $\nu = 0.3$.

Since a number of pores are present, the uniaxial stress in volume V_2 will have a value of τ, larger than the nominal stress S because of the decrease in cross-sectional area due to the pores. Denoting the volume fraction of pores by $P = NV_o/V$ it may be shown that $\tau = \left\{1/(1-P)\right\}\, S$.

From the preceding results one could attempt to predict the strength of a porous ceramic by dividing the strength of the zero porosity

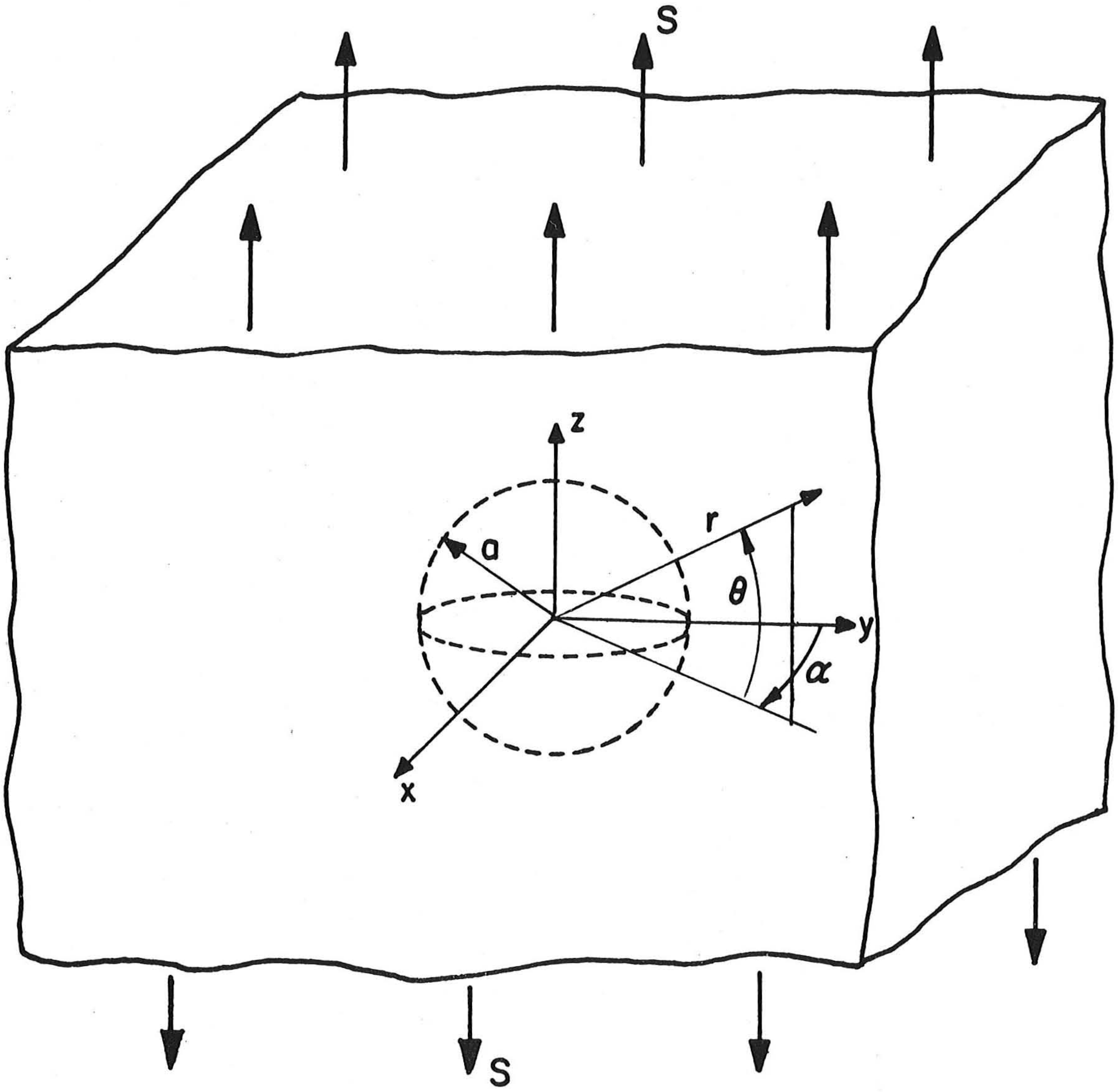

XBL 7512-9461

Fig. 2. Coordinate system used to describe stress state around a spherical hole.

material by the effective stress concentration factor. However, this approach greatly underestimates the strength of the porous material and sheds no light on the observed variation of strength with porosity. For this reason Finnie and Vardar[11] turned to the Weibull probabalistic approach to brittle strength which allows them to consider the effect of the stressed volume, as well as the stress level, on the probability of failure.

1. The Weibull Statistical Approach

For uniaxial stress states, Weibull[9] took the probability of failure as

$$F(\sigma) = 1 - \exp - \left[\int (\sigma/\sigma_o)^m \, dV\right] \tag{12}$$

with the integral being taken over the region stressed in tension. The parameters m and σ_o which are assumed to characterize a given material may be obtained, for example, from bending test data.

For multiaxial stress states such as shown in Fig. 3 [taken from Ref. (10)], Weibull wrote the cummulative distribution of failure probability as:

$$F(\sigma) = 1 - \exp[-B] = 1 - \exp \left[-\int \Big(K \int_{\substack{A \\ \text{unit} \\ \text{sphere}}} \sigma_n{}^m dA\Big) dV\right] \tag{13}$$

where the normal stress at each point on the unit sphere is

$$\sigma_n = \cos^2\phi \, (\sigma_1 \cos^2 \psi + \sigma_2 \sin^2 \psi) + \sigma_3 \sin^2 \phi; \; dA = \cos \phi \, d \psi \, d \phi$$

and the integration is limited to the range of angles for which σ_n is tensile. Thus, in the present problem they had to carry out the integration over unit spheres, throughout the volumes V_1 and V_2. The

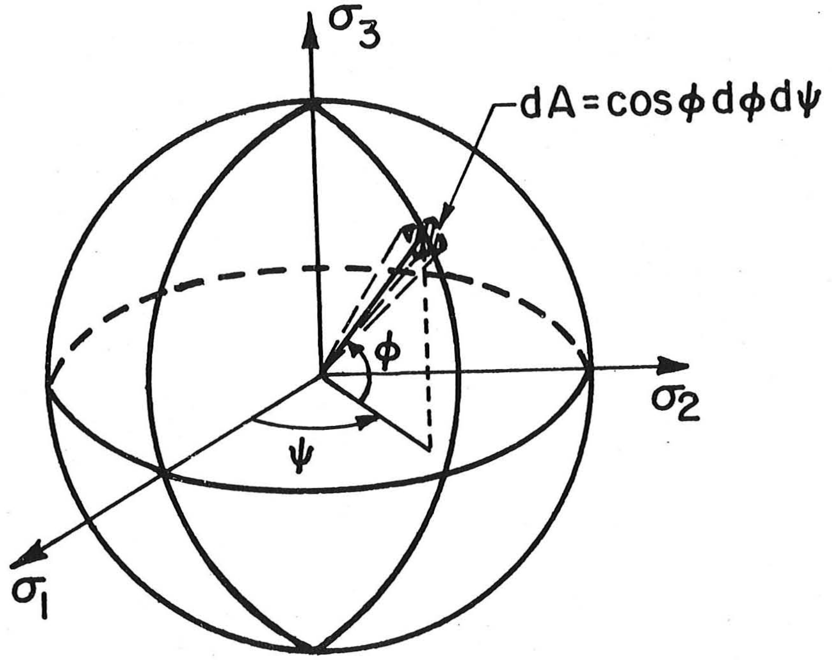

XBL 7512-10,009

Fig. 3. Geometric variables used to describe location on a unit sphere.

quantity B in Eqn. 13 is then

$$B = \int_{V_2} \Big[K \int_{\substack{A \\ \text{unit} \\ \text{sphere}}} (\sigma_3 \sin^2\phi)^m \cos\phi \, d\psi \, d\phi\Big] \, dV + N \int_{V_1} K \int_{\substack{A \\ \text{unit} \\ \text{sphere}}} G(r,\theta,\phi,\psi) \, d\phi \, d\psi \, d\theta \, d\alpha \, dr$$

where G is a function to be defined later.

The first integral is for the region of uniaxial stress and presents no problem. Putting $\sigma_3 = \tau$ and using the uniaxial formulation it is merely $V_2(\tau/\sigma_o)^m$. The second integral can be written in detail as:

$$Na^3K \int_{r/a}\int_{\theta}\int_{\alpha} \left\{ \int_{\psi}\int_{\phi} \left[\sigma_1^2\cos^2\psi\cos^2\phi + \sigma_2^2\sin^2\psi\cos^2\phi + \sigma_3\sin^2\phi\right]^m \cos\phi \, d\phi \, d\psi \right\} (r/a)^2 \cos\theta \, d\theta \, d\alpha \, d(r/a)$$

Where a is the pore radius and the upper limit of integration on r/a, corresponding to volume V_1 has to be specified. The stresses σ_1, σ_2, σ_3, vary with location θ and r/a, but for a given Poisson's ratio depend only on θ and r/a. Thus, for a given upper limit of integration on r/a

$$B = V_2 \left(\frac{\tau}{\sigma_o}\right)^m + Na^3K\tau^m H(m)$$

Letting λ denote the upper limit of r/a, i.e. λa is the radius of region V_1, we have $V_2 = V - NV_1 - NV_o = V(1-P\lambda^3)$.

Then, $$B = V(1-P\lambda^3)\left[\frac{S}{\sigma_o(1-P)}\right]^m + \frac{3V}{4\pi} KP \left[S/(1-P)\right]^m H(m)$$

where H(m) will depend on the choice of λ. Comparing with the uniaxial formulation*

$$K = \frac{2(2m+1)}{\pi\sigma_o^m}$$

So $$B = \left(\frac{S}{\sigma_o}\right)^m V \left\{ \frac{1}{(1-P)^m} \left[(1-P\lambda^3) + \frac{3(2m+1)}{2\pi^2} PH(m)\right] \right\} = \left(\frac{S}{\sigma_o}\right)^m V\{A\} \qquad (14)$$

---

*This differs by a factor 4 from the value given on P. 497 of Ref. 10 because here they took advantage of symmetry to integrate only over one quarter of the unit sphere.

Taking a span L between outer supports and a span of $L-2\ell$ between inner supports ($L-2\ell = 0$ for 3-point bending) one may use the Weibull uniaxial formulation for 4-point bending, treat the problem as if pores were not present, and then multiply by the quantity between parenthesis $\{A\}$ in Eqn. 14. Thus if S is taken as the maximum, outer fiber, tensile stress in bending one obtains an expression for B by multiplying the preceding equation by $\left[\{(m+1)/2\} - m\ell/L\right] / (m+1)^2$.

To minimize computation it is more convenient to work with the median strength in a bending test rather than the mean. In this case B = .693 and

$$\frac{S\ \text{median}}{\sigma_o} V^{1/m} = \left(\frac{.693}{\{A\}}\right)^{1/m} \left(\frac{(m+1)^2}{\left(\frac{m+1}{2}\right) - \frac{\ell m}{L}}\right)^{1/m} \tag{15}$$

The computation was carried out by Finnie and Vardar[11] using the upper value of λ for r/a corresponding to volume V_1.

Since $\{A\}^{1/m}$ is the quantity involved in strength predictions, they decided that a value of $\lambda = 2.02$ was adequate for subsequent calculations. This choice, which was a reflection of the rate of decay of stresses with r/a, limited the analysis based on isolated spherical holes to a porosity of about 10%.

Having selected a value for λ, the numerical evaluation of Eqn. 15 could be presented in the concise form shown in Fig. 4. The effect of Poisson's ratio was evaluated only for m = 4 and m = 20 and is seen to be fairly insignificant. A low value of m indicates a material containing flaws of highly variable severity and a high value indicates a material with uniform distribution of flaws of similar geometry. This

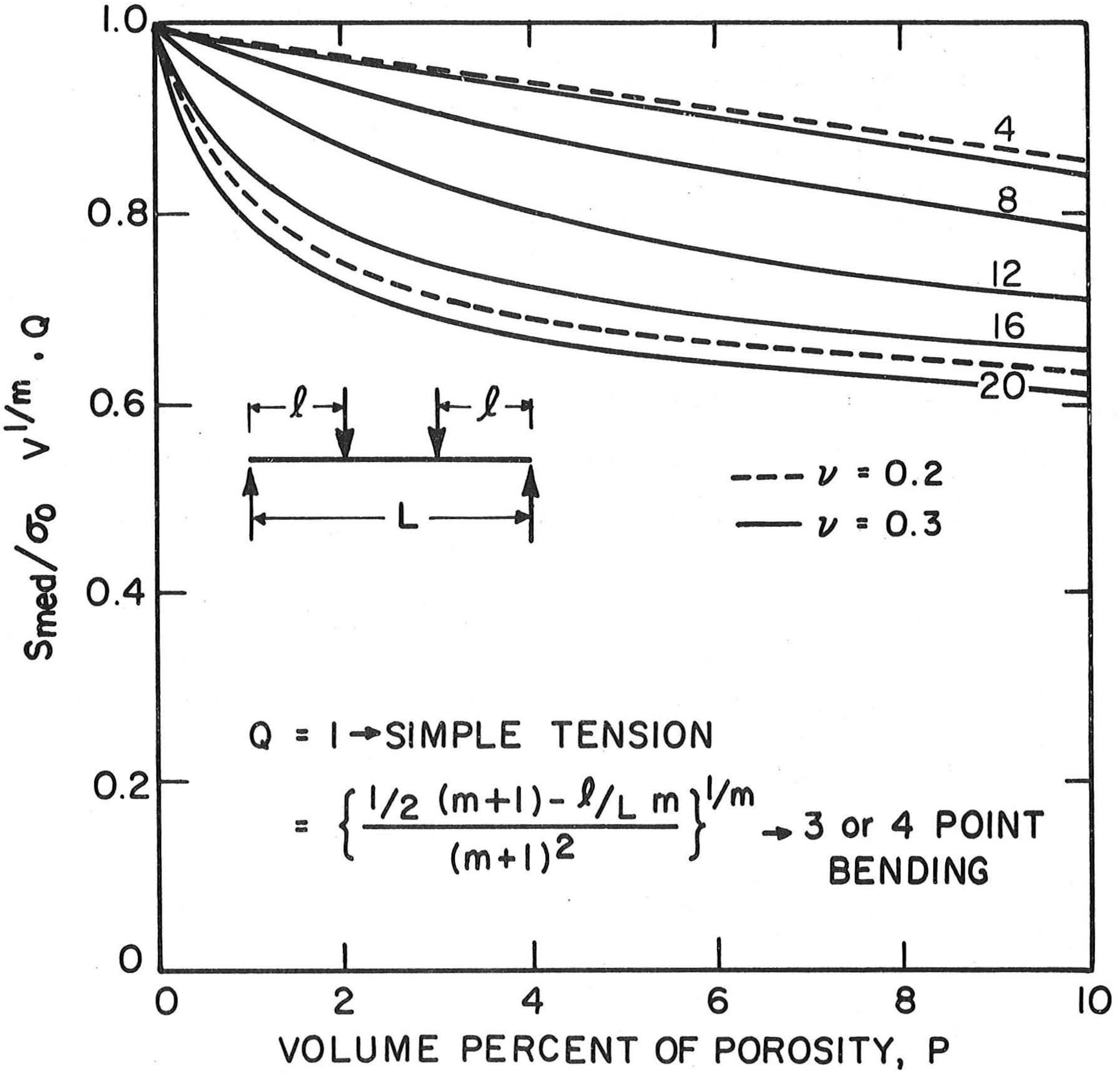

XBL 768-7457

Fig. 4. Predicted variation of median strength as a function of porosity for values of the Weibull parameter m as shown on curves.

model will be tested with the present experimental results and discussed in the results and discussion section.

B. Porosity and Elastic Modulus

The elastic modulus of ceramics varies markedly with porosity but does not depend upon pore size, grain size, or surface conditions. A number of theoretical attampts have been made to calculate the elastic properties of porous bodies. The equation for the shear modulus (G) proposed by MacKenzie[13] was

$$G/Go = 1 - AP + BP^2 \tag{16}$$

where Go is the shear modulus at zero porosity, P is the porosity and A and B are constants. Hashin[14] proposed a relationship for multiphased bodies which as pointed out by Hasselman[15] reduces to

$$\frac{G}{G_o} = 1 + \frac{AP}{1-(A+1)P} \tag{17}$$

for a porous body where A is a constant. Spriggs[16] proposed for Al_2O_3 that his experimental data followed an empirical relation

$$E = E_o \exp^{-bP} \tag{18}$$

where E_o is the Young's modulus at zero porosity and b is a constant. Knudsen[17] showed that all data for Al_2O_3 could be approximated by a value of b equal to 3.95.

In dealing with many ceramic materials[7] the expression

$$E/E_o = 1 - KP \tag{19}$$

where K is a constant, gives a linear relationship between elastic modulus and porosity. Hasselman and Fulrath[18] studied the effect of spherical porosity on the elastic modulus of glass at low porosities.

Their results clearly demonstrated that at low porosities (<3%) a linear relationship is observed which is in agreement with the theoretical predictions of MacKenzie[13] and Hashin[14] at low porosities, i.e., Equations (16) and (17) give linear approximations when P is small.

III. FRACTURE MECHANICS PARAMETERS FOR CERAMIC MATERIALS

In recent years the measurement of fracture mechanics parameters for ceramic materials has received increasing attention. The definition of fracture mechanics parameters and their measuring techniques appropriate to the present study are breifly discussed below.

Lead zirconate-titanate ceramics exhibit brittle fracture. For brittle materials, failure occurs when the normal stress in the vicinity of a crack tip reaches a critical value for bond rupture. For a meterial containing a sharp crack of length 2a subjected to an applied stress, σa, the stress intensification at the crack tip (K_I) is related to σ_a by[19]

$$K_I = \sigma_a Y \sqrt{a} \tag{20}$$

where Y is a dimensional constant depending on the geometry of loading and crack configuration. When fracture occurs exclusively by the opening mode and plane strain conditions exist at the crack tip, the value of K_I for fast fracture is the critical stress intensity factor K_{IC} (fracture toughness), a material parameter.[20] Another inportant fracture mechanics parameter is fracture surface energy, γ_F, which is related to K_{IC} as,

$$\frac{K_{IC}^2(1-\nu^2)}{E} = G_{IC} = 2\gamma_F \tag{21}$$

where G_{IC} is the strain energy release rate - defined as the work required to create unit increase in crack area by fracture, E is the elastic modulus and ν is the Poisson's ratio. G_{IC} is twice the value of γ_F deduced from a fracture test because the crack produces two surfaces. Although γ_F is often determined for ceramic materials, K_I values are most convenient and directly applicable to failure prediction. The specimens that are used extensively for room temperature measurements are the bend specimen,[21] compact tension specimen,[21] double cantilever beam specimen[22] and double torsion specimen.[20] The constant K specimens[19,21] where crack length is independent of K_I values are extensively used in ceramic systems. The reason for this is that the accurate measurement of flaw length by dye penetrant or optical procedures is very difficult. Therefore, for these materials or any other materials where measurement of flaw length is difficult, it is essential that flaw length measurements are eliminated. At ambient temperature, the double torsion method is convenient for measuring K_{IC} values and was used in the present investigation to get the K_{IC} values for PNZT ceramics. Once K_{IC} values and the elastic modulus are available the critical strain energy release rate G_{IC} and fracture surface energy γ_F can be easily calculated by using Equation(21).

IV. EXPERIMENTAL PROCEDURES

A. Preparation of Powders and Fabrication of Specimens

The material used in this study was lead zirconate-titanate in which the grain size was controlled by doping with one mole percent Nb_2O_5. The composition of PZT doped with Nb (PNZT) ceramic used was $Pb_{0.99}\square_{0.01}\left(Zr_{0.52}\,Ti_{0.46}\,Nb_{0.02}\right)O_3$ where $\square$ is a lead vacancy. The raw powders of PbO, ZrO_2, TiO_2 and Nb_2O_5 were milled in a vibratory energy mill for 4 hours using isopropyl alcohol as a liquid medium, then dried and calcined at 850°C for 4 hours (Fig. 5). The powders were passed through -20 mesh screen and mixed with excess* PbO and finally milled for 4 hours using isopropyl alcohol and a polyvinyl alcohol, water solution and then air dried. The polyvinyl alcohol was added as a pressing aid and binder.

The detailed fabrication procedure of PNZT ceramics containing artificially introduced large pores (spherical and acicular) is shown in Fig. 6. The specimens containing fine pores comparable to the grain size were fabricated by varying the sintering conditions (viz. green density, sintering time and temperature). In both cases, the specimens were buried in $PbZrO_3 + ZrO_2$ (PZ + Z) packing powder and fired in one atmospheric pressure of oxygen. The packing powder technique was used to control PbO loss from the specimen during sintering. The processing of PZ+Z packing powder is shown in Fig. 7.

---

*There were two starting powder compositions used in this study. One contained 5.5 w/o excess PbO (used for fracture strength and elastic modulus measurement) and the other one contained 1 w/o excess PbO (used for fracture toughness measurement). During sintering the excess PbO was evaporated to the packing powder. However, it greatly enhanced the sintering in the early stages by providing a transient liquid phase.

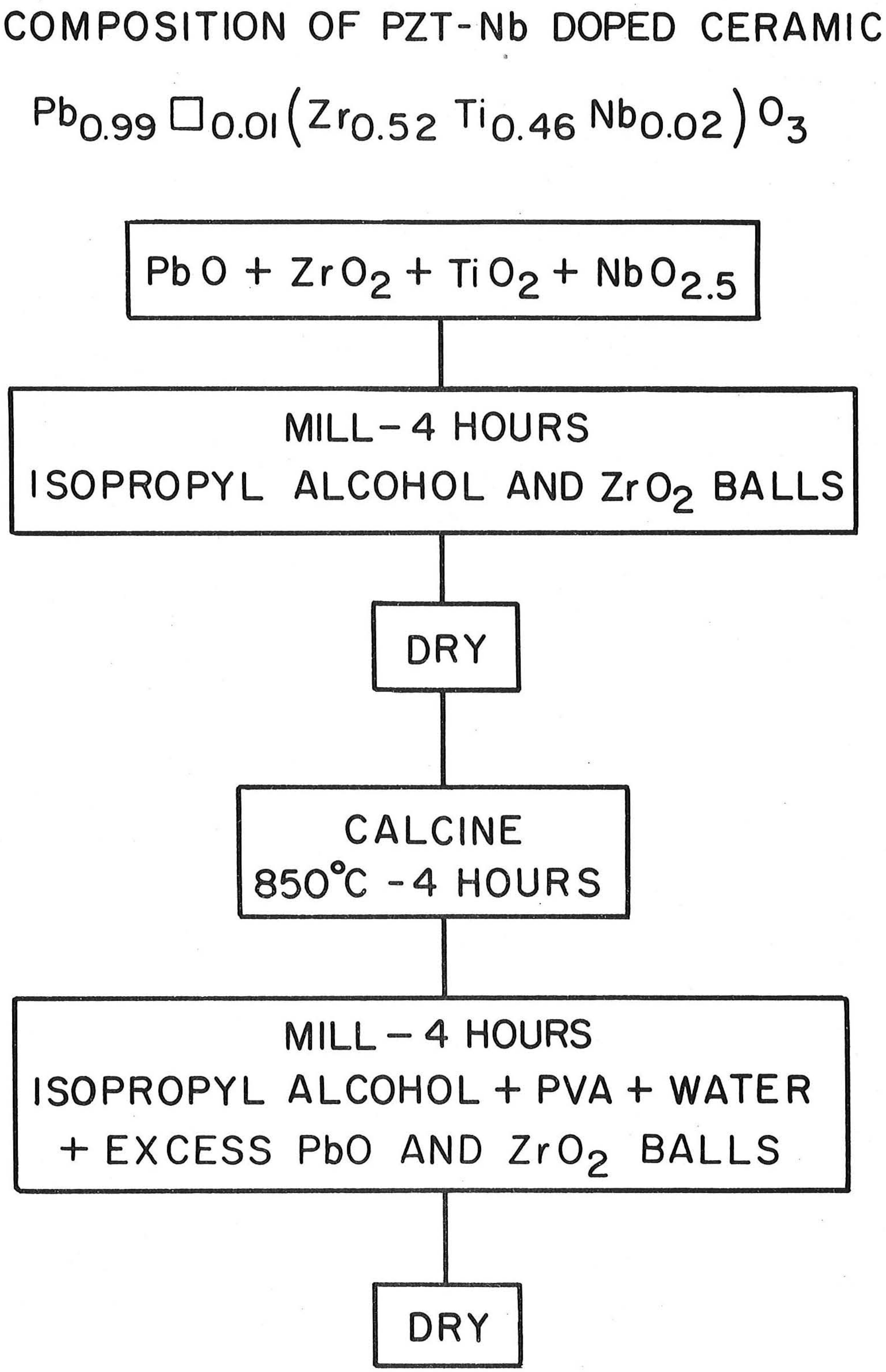

XBL 759-7374A

Fig. 5. Processing diagram for PNZT powders.

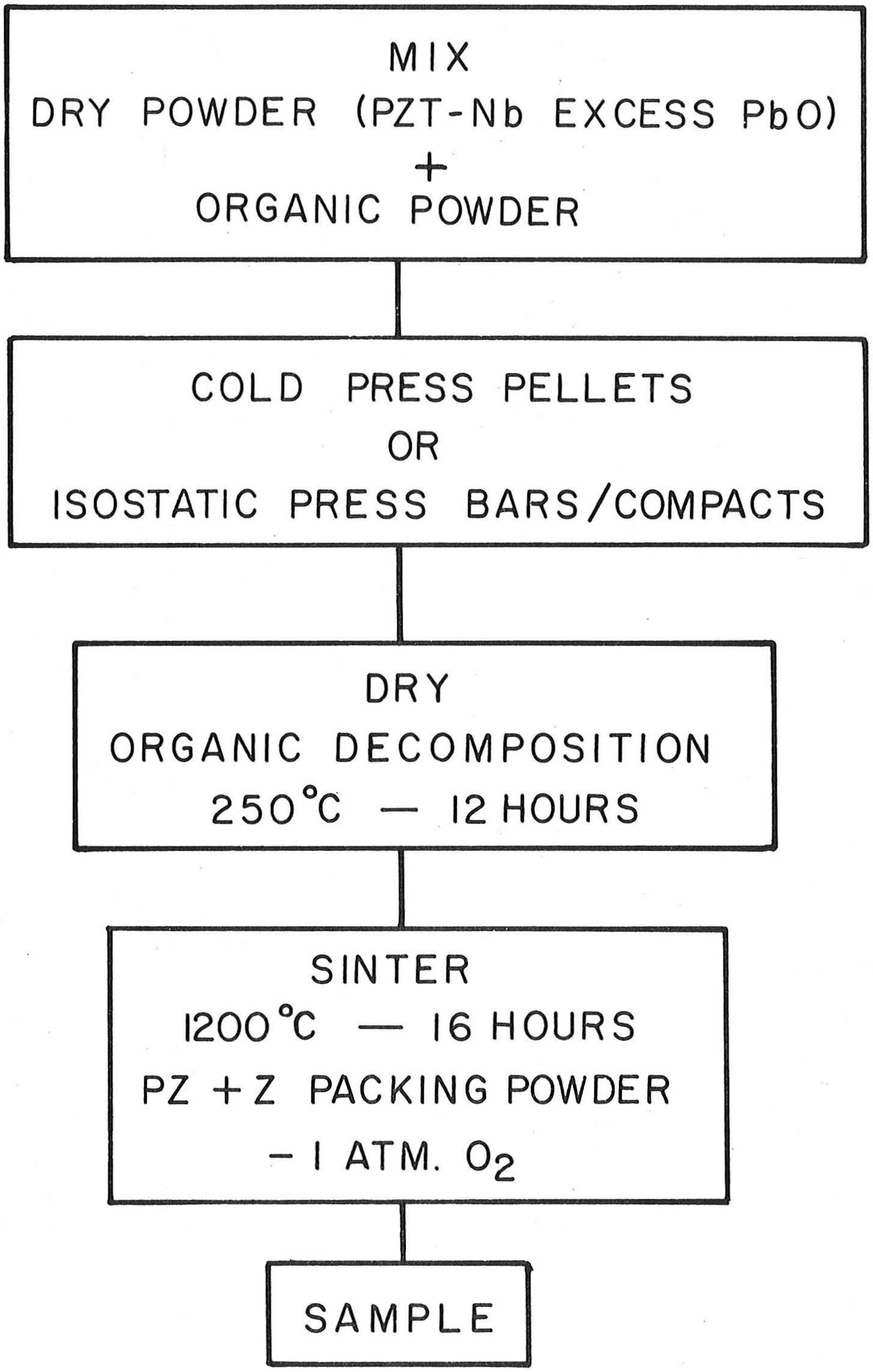

XBL766-7029

Fig. 6. Fabrication diagram for PNZT samples.

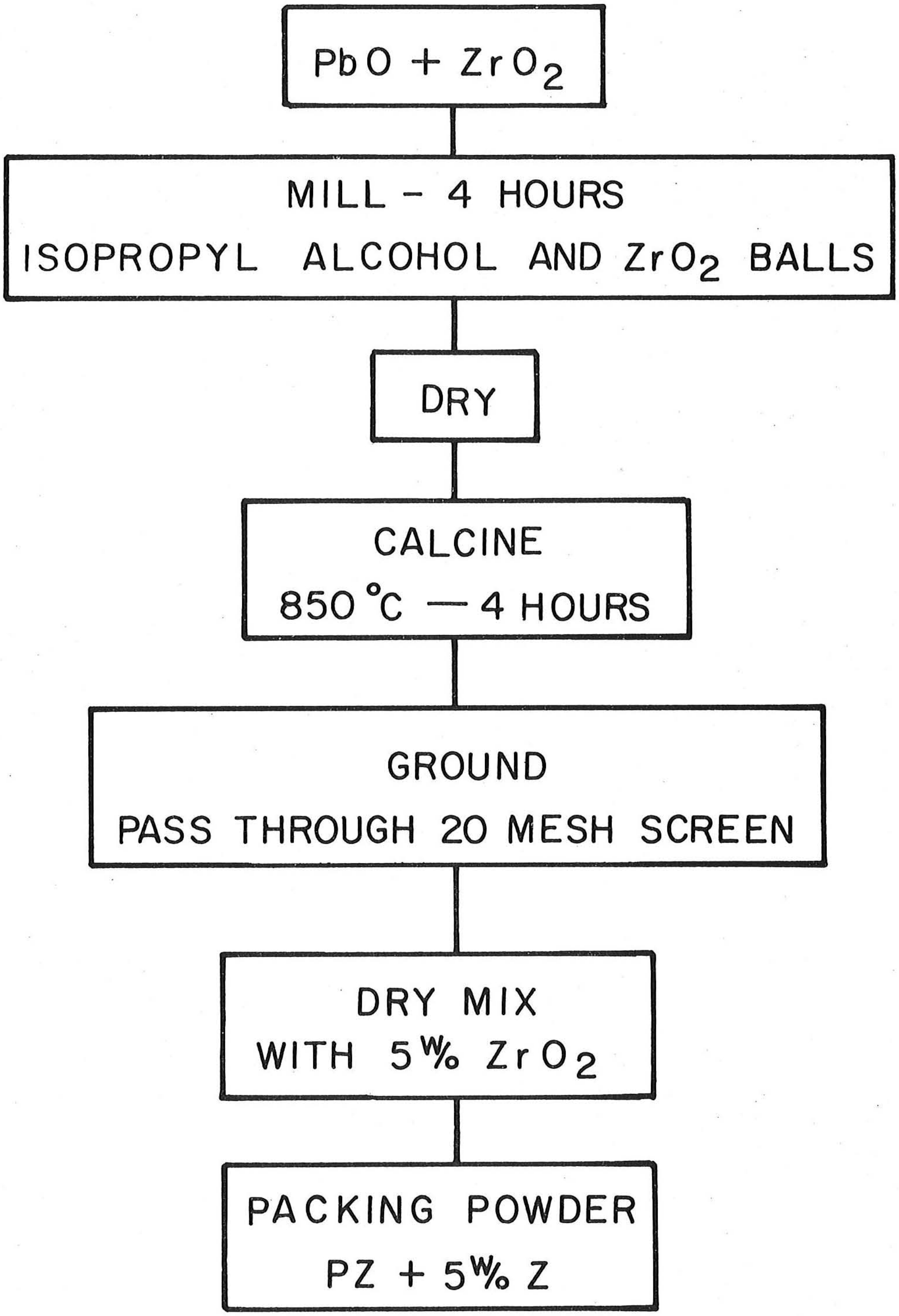

XBL 766-7030

Fig. 7. Processing diagram for PZ + Z packing powder.

B. Density Measurements

The apparent density of PNZT specimens was determined from dry and suspended weights in isopropyl alcohol relative to a nickel metal standard. Calculation of the density of the specimen was done by using the expression,

$$\rho_{\text{specimen}} = \left[\frac{W_D}{W_D - W_S}\right]_{\text{Specimen}} \times \left[\frac{W_D - W_S}{W_D}\right]_{\text{Standard}} \times \rho_{\text{Standard}} \qquad (22)$$

where W_D is the dry weight, W_S is the saturated suspended weight and ρ_{standard} is the density of Ni taken to be as 8.91 gms/cc. The theoretical density of PNZT ceramic was taken as 8.00 gm/cc. The bulk density of PNZT-fine pore specimens was calculated from the dry weight and the dimensions.

C. Mechanical Property Measurement

1. Fracture Strength

The sintered pellets,* were cut into strength specimens approximately 0.05 in. thick with a precision diamond saw using kerosene as a coolant. The length and width of the specimens were approximately 1.0 in. and 0.3 in. respectively. Uniaxial bend strength was determined by loading the specimens to failure using a simple 4-point bending machine (Fig. 8) with 0.75 in. overall span and 0.25 in. inner span. The diamond sawed surface was stressed. The fracture strength was calculated from the following equation

$$\sigma = \frac{PL}{bd^2} \qquad (23)$$

where σ is the maximum stress fracture, L is the overall span, b is the

*Containing artificially introduced pores and fine pores.

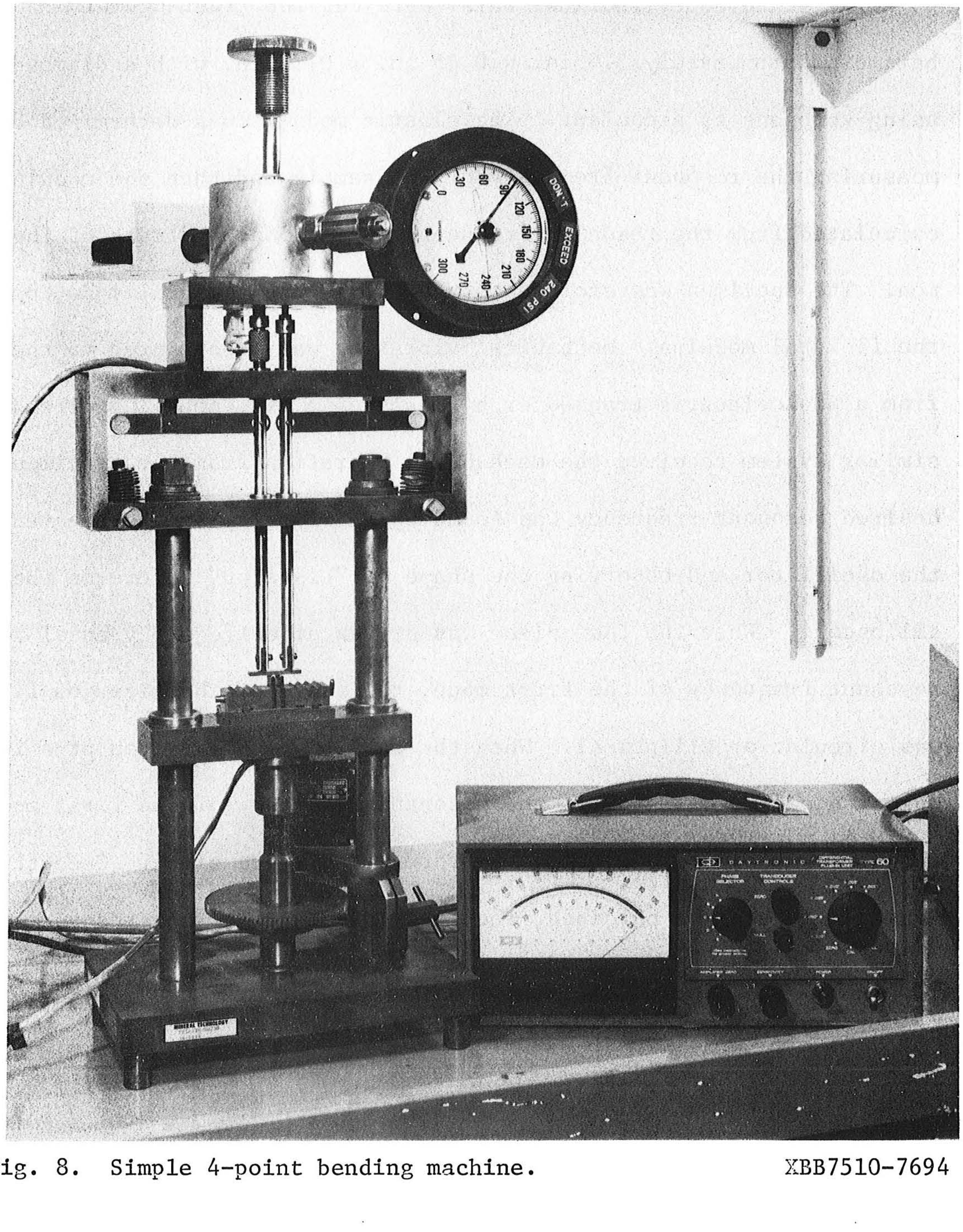

Fig. 8. Simple 4-point bending machine. XBB7510-7694

width and d is the thickness of the specimen. The width and thickness were measured at the point of fracture.

2. Elastic Modulus and Damping Capacity

The sintered cylindrical bars* were cut into rectangular bars of approximately 3.0 in. x 0.25 in. x 0.20 in. with a diamond saw using kerosene as a coolant. The elastic modulus was determined by measuring the resonant frequency of the sample and then the modulus was calculated from the resonant frequency, dimensions and mass of the specimen. The specimen was excited to vibrate in the flexural mode to obtain the flexural modulus. Mechanical vibration was transmitted to the sample from a piezoelectric transducer by means of a fine coupling wire and a similar system received the mechanical vibration from the specimen. The desired resonant frequency was found by slowly varying the frequency of the oscillator and observing the shape of "Lissajou" figure on the oscilloscope. When the test piece was driven at a frequency equal to the resonant frequency of the first mode, the shape of the Lissajou figure was circular or elliptical. When the test piece was driven at a frequency equal to one-half of the resonant frequency of the first mode, the Lissajou figure showed in the form of a figure eight. Once the exact frequency was obtained, the Young's modulus to the resonant frequency of the first mode of flexural vibration of a rectangular bar was calculated from the expression[23]

$$E = 0.94645 \frac{Cmf^2}{B} \qquad (24)$$

where m is the mass of the specimen, f is the resonant frequency of the first mode of flexural vibration, B is the dimension of cross-section

*Containing artificially introduced porosity and fine pores.

perpendicularly to the direction of vibration and C is the shape factor defined by

$$C = (D/L)^{-3}\left[1+6.585\ (1+0.0752\nu + 0.08109\nu^{2})(D/L)^{2} - \frac{100.\ 083\ (1+0.2023\nu + 2.173\nu^{2})\ (D/L)^{4}}{12 + 76.06(1+0.1408 + 1.536\nu^{2})\ (D/L)^{2}} - 0.86806(D/L)^{4}\right]$$

where D is the dimension of the cross-section parallel to the direction of vibration, L is the length of the specimen and ν is the Poisson's ratio. The value of C was taken from the tables[23] generated by Hasselman.

Damping capacity was determined from the width at the half-maximum value of the resonance curve. The value was obtained by finding the resonant frequency at the maximum amplitude and then locating the two frequencies above and below the resonant frequency at which the amplitude decreased to half of the resonance amplitude. Damping capacity δ was then calculated from the differences of the two frequencies Δf and the resonant frequency f as

$$\delta = 1.8136\ \frac{\Delta f}{f} \tag{25}$$

3. Fracture Toughness

The double torsion specimen configuration is given in Fig. 9 along with the crack front curvature in the lower portion of Fig. 9. The nominal dimensions of the specimen were approximately 2.0 in. in length x 1.0 in. width x 0.08 in. thick. The side groove of depth ~0.04 in. was introduced by using a 0.02 in. thick diamond blade and the precracking was done by a 0.008 in. thick diamond blade. The specimens were loaded in a 4-point bending machine. The specimens failed catastrophically and the load at the point of failure was noted as P. K_I was calculated from

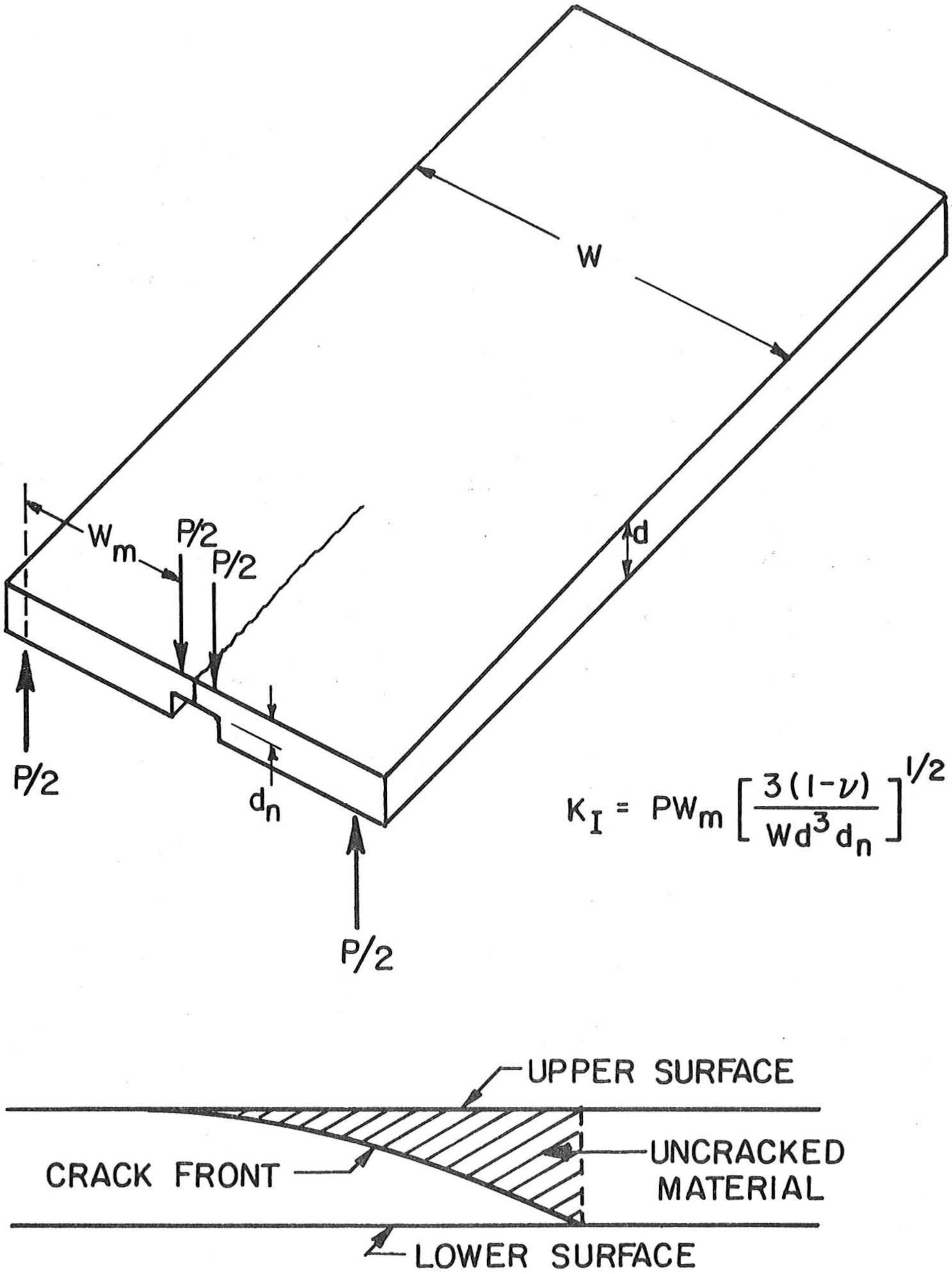

XBL 766-7026

Fig. 9. The double torsion specimen and the crack front curvature is shown in the lower part of the figure.

the following expression derived by Williams and Evans,[24]

$$K_I = PW_m \left[\frac{3(1+\nu)}{Wd^3 d_n}\right]^{1/2} \tag{26}$$

where ν is the Poisson's ratio taken to be as 0.29 for PNZT ceramics and W, W_m, d and d_n are the specimen dimensions as shown in Fig. 9. The critical stress intensity factor or the fracture toughness depends only on the applied load P and not on the crack length. It should be noted that this K_I value is obtained from G_I value calculated by a compliance analysis. Hence, it represents an average K_I over the curved crack front.

The microstructures, fracture surfaces and fracture origin were observed by scanning electron microscopy.

V. RESULTS AND DISCUSSIONS

A. Fracture Strength

The fracture strength of three series of PNZT ceramic specimens was measured by 4-point bending. The first series (PNZT-Spherical Pore) consisted of a highly dense PNZT matrix containing a controlled amount of spherical porosity with varying pore size. The grain size was much smaller than the pore size. The pores were acicular in the second series of the specimens in which the grain size was also much amaller than the pore size. The final series of specimens had the pore size in the same range as the grain size (PNZT- fine pore). The starting powder (PNZT + 5 w/o excess PbO) was the same for all series but in the case of PNZT-fine pore specimens, the sintering conditions (mainly sintering temperature and time) were varied to generate different amounts of fine porosity. The excess PbO forms a lead oxide rich liquid at around 880°C and during sintering at 1200°C for 16 hours (in case of PNZT - spherical and acicular pore specimens), most of this excess PbO would evaporate to the packing powder. In case of PNZT - fine pore specimens (fired at low temperature, 1100° to 1150°C), it is suspected that some remaining PbO rich liquid would be converted to crystalline PbO and PNZT during cooling and remains in the grain boundaries. This would give a different grain boundary structure for the PNZT - fine pore specimens.

In a bend test, the maximum tensile stress is in the outer fibers of the specimen. When the tensile stress reaches a critical value near a pore or a flaw generated by diamong sawing, failure occurs.

The fracture strength of PNZT - spherical pore specimens is shown in Table I and the plot of fracture strength against the volume percent

Table I. Fracture Strength of PNZT - Spherical Pore Ceramics

Volume Percent Porosity	Pore Size µm	Mean Fracture Strength σ_{mean} PSI	Median Fracture Strength σ_{med} PSI	$\frac{\sigma_{med}}{\sigma_o}$
-	-	12,000 ± 4.9%	12,000	1.00
2.50	25-40	9,250 ± 5.9%	9,180	0.765
2.50	60-75	9,540 ± 8.7%	9,630	0.802
2.90	110-150	9,290 ± 5.0%	9,345	0.780
4.70	25-40	7,850 ± 11.8%	7,945	0.660
4.65	60-75	8,350 ± 5.7%	8,290	0.690
4.85	110-150	7,650 ± 4.4%	7.590	0.630
8.80	25-40	7,410 ± 5.0%	7,450	0.620
9.10	60-75	7,720 ± 7.1%	7,830	0.650
8.95	110-150	7,150 ± 12.2%	6,800	0.570
11.70	25-40	6,930 ± 3.1%	6,900	0.575
12.60	60-75	7,500 ± 6.7%	7,720	0.625
13.50	110-150	7,040 ± 7.5%	7,270	0.585

porosity is shown in Fig. 10. The fracture strength decreases rapidly with the initial increase in porosity and then levels off at around 8% porosity. The experimental results were analyzed using the Weibull's probabilistic approach to brittle strength as described earlier. Because the specimens have the same volume and the value of Q in Fig. 4 is unchanged, the normalized strength was used directly to estimate the effect of porosity on the median strength.[25] Figure 11 shows the experimental results (normalized strength vs. porosity from Fig. 10) and the predicted curve based on the Weibull approach. Poisson's ratio[26] was assumed to be equal to 0.29 for PNZT. The curve for $m = 20$ and $\nu = 0.3$ is shown in Fig. 11. Also shown in Fig. 11 are the predictions for the relative strength obtained by considering only the decrease in cross-sectional area and that obtained by combining the stress concentration factor and the decrease in cross-sectional area. The effect of spherical pore size is insignificant when the pore size is much larger than the grain size. A typical distribution of spherical pores is shown in Fig. 12a. Figure 13 shows the microstructure of the dense PNZT matrix. The pore size range reported in this study was calculated by considering the initial organic particle size after screening and the shrinkage of the specimen (about 15% for all specimens) during sintering. The grain size was calculated by the line intercept method.

For the PNZT - acicular pore system, the fracture strengths are given in Table II and a plot of the fracture strength against the volume percent porosity is shown in Fig. 10. The fracture strength decreases rapidly with increase in porosity and then levels off at around 5% porosity. The distribution of acicular pores in the PNZT matrix is shown

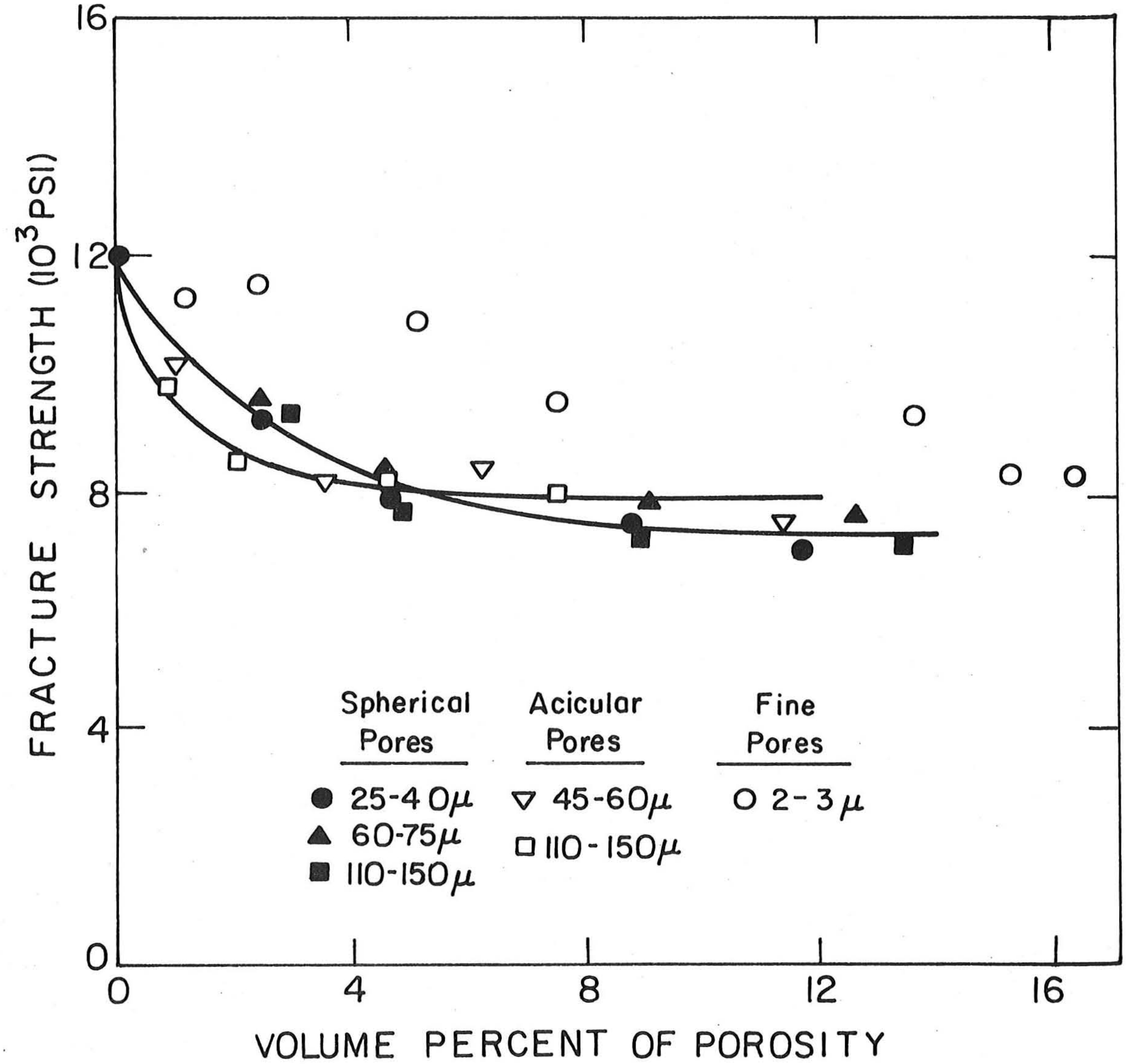

XBL 7512-10,007A

Fig. 10. Fracture strength of PNZT ceramics containing spherical pores, acicular pores and fine pores against the volume percent of porosity.

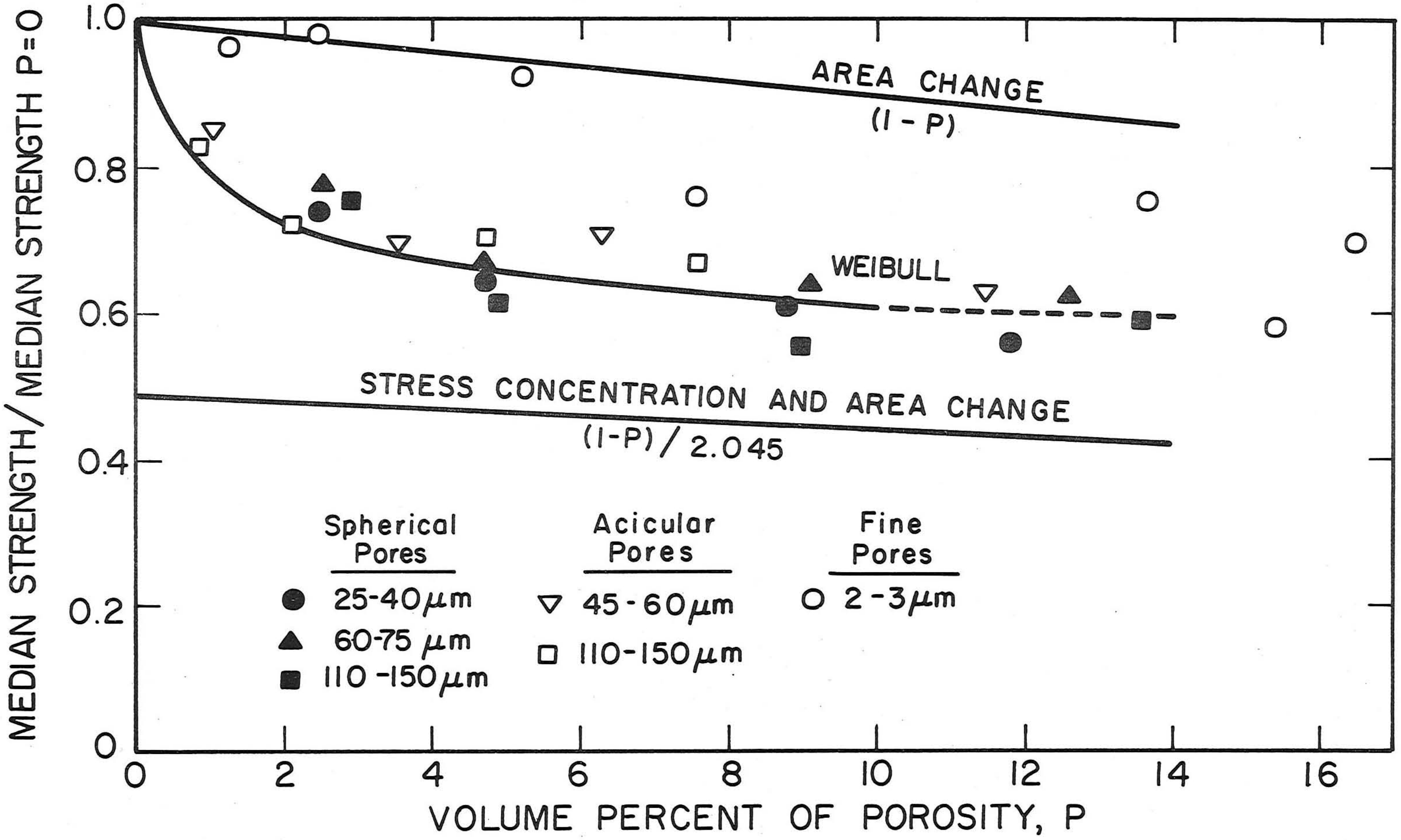

XBL 768-7458

Fig. 11. Predicted and observed ratio of median strength with porosity to median strength with zero porosity. The prediction of Fig. 4 is extrapolated for values over 10%.

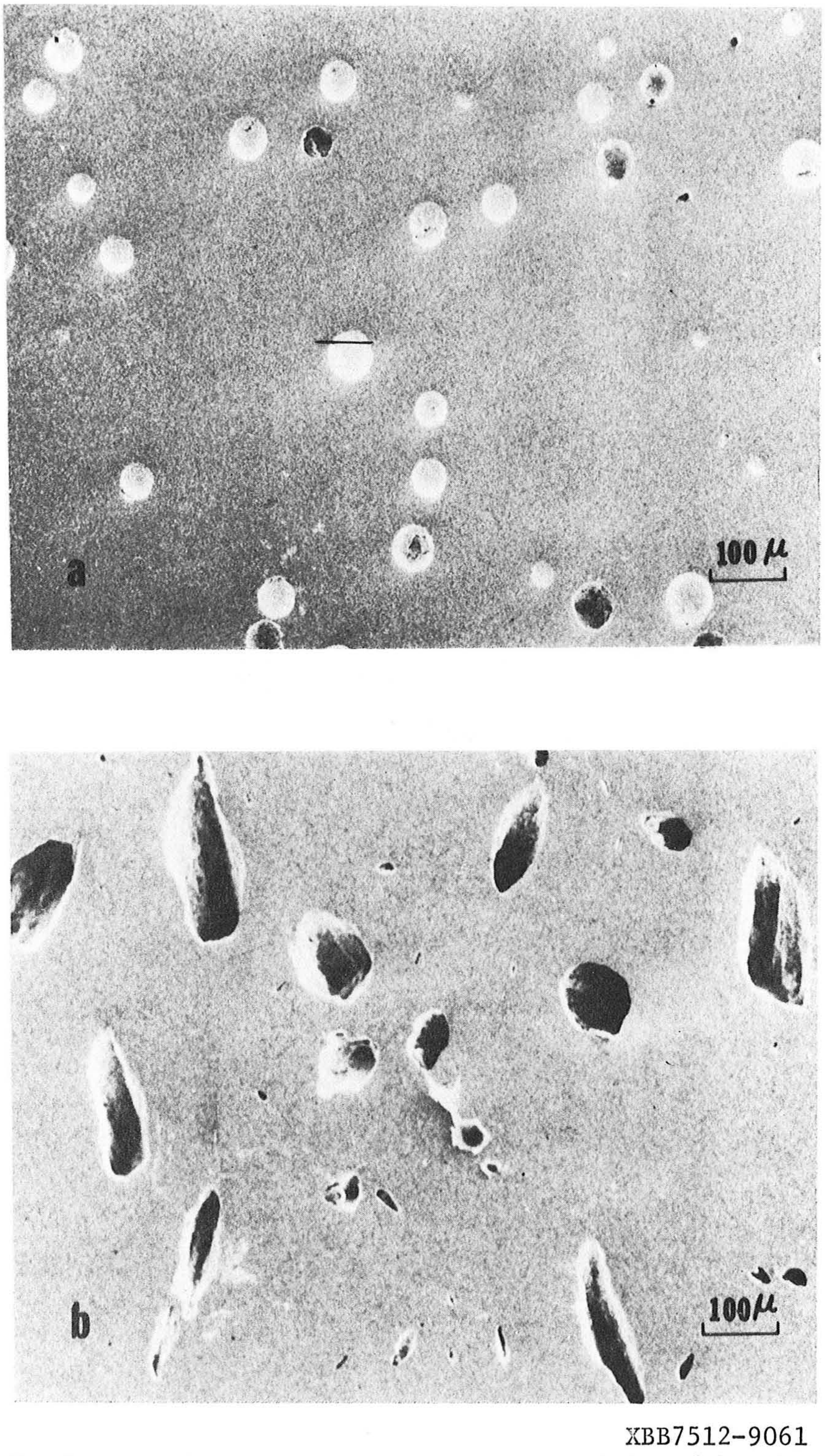

XBB7512-9061

Fig. 12. Random section of PNZT specimens containing (a) spherical pores (4.65% porosity, 60-75 μm pore size), and (b) acicular pores (4.65% porosity, 110-150 μm pore size).

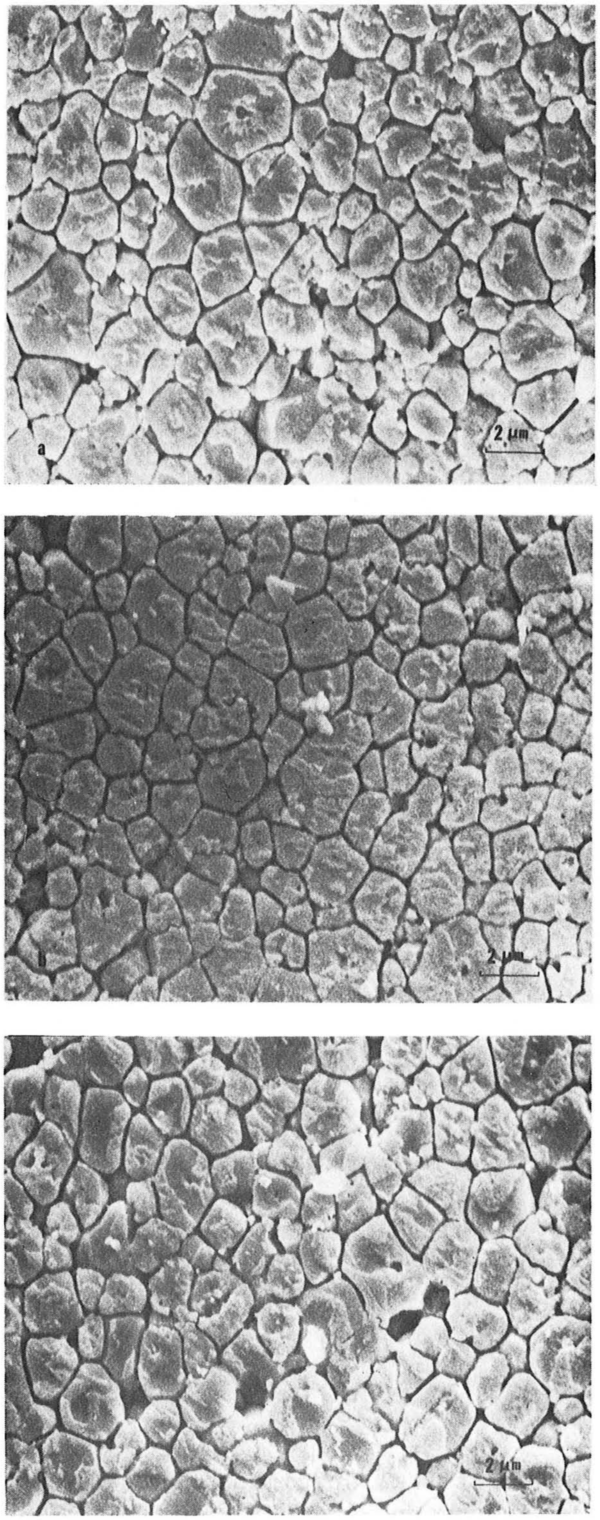

XBB7510-7489

Fig. 13. Typical microstructures of three different PNZT matrix materials showing the uniformity in grain size.

Table II. Fracture Strength of PNZT Acicular Pore Ceramics

Volume Percent Porosity	Pore Size μm	Mean Fracture Strength, σ_{mean} PSI	Median Fracture Strength, σ_{med} PSI	$\frac{\sigma_{med}}{\sigma_o}$
1.05	45-60	10,140 ± 3.8%	10,140	0.845
3.55		8,150 ± 7.2%	8,325	0.694
6.25		8,390 ± 5.6%	8,485	0.707
11.40		7,460 ± 2.2%	7,510	0.626
0.87	110-150	9,775 ± 7.9%	9,935	0.828
2.10		8,415 ± 10.0%	8,560	0.713
4.66		8,165 ± 8.5%	8,280	0.690
7.51		7,925 ± 6.3%	8,050	0.670

in Fig. 12b. From Fig. 11, it is clear that the fracture strength of PNZT - acicular pore system also follow the Weibull's probabilistic approach. Here also, the fracture strength is independent of acicular pore size (grain size is much smaller than the pore size).

For the PNZT - fine pore ceramics, the fracture strength are given in Table III and the results are shown in Figs. 10 and 11. The experimental results follow the prediction for relative strength obtained by considering only the cross-sectional area change up to approximately 5% porosity. Up to 5% of fine porosity, the strength shows higher values than those specimens where pore size are much larger than the grain size. Figure 14 shows the size and distribution of fine pores formed by varying the sintering conditions. The pore size was measured by the line intercept method. The grain size changes with change in sintering conditions are shown in Fig. 15. Typical fracture surfaces of fine pore specimens are shown in Fig. 16. The pore size and grain size for all PNZT ceramics are summarized in Table IV.

B. Fractographic Analysis

In polycrystalline ceramic materials, the propagating cracks typically spread on more than one plane due to intergranular or combined intergranular and transgranular fracture. This motion generates markings on the fracture surface which show up as "river patterns" and provides an excellent means for determining the direction of crack propagation. In some cases the river pattern can be traced back to determine the fracture origin. After fracturing the PNZT ceramics, the fracture surfaces were observed by scanning electron microscopy. The fracture

Table III. Fracture Strength of PNZT Fine Pore Ceramics

Volume Percent Porosity	Mean Fracture Strength, σ_{mean} PSI	Median Fracture Strength σ_{med} PSI	$\frac{\sigma_{med}}{\sigma_o}$
1.20	11,225 ± 8.6%	11,550	0.962
2.40	11,520 ± 6.4%	11,860	0.988
5.16	10,870 ± 4.4%	11,080	0.923
7.50	9,250 ± 10.8%	9,020	0.752
13.63	9,230 ± 9.6%	9,060	0.755
15.33	8,270 ± 5.0%	8,185	0.682
16.40	8.270 ± 7.0%	8,475	0.706

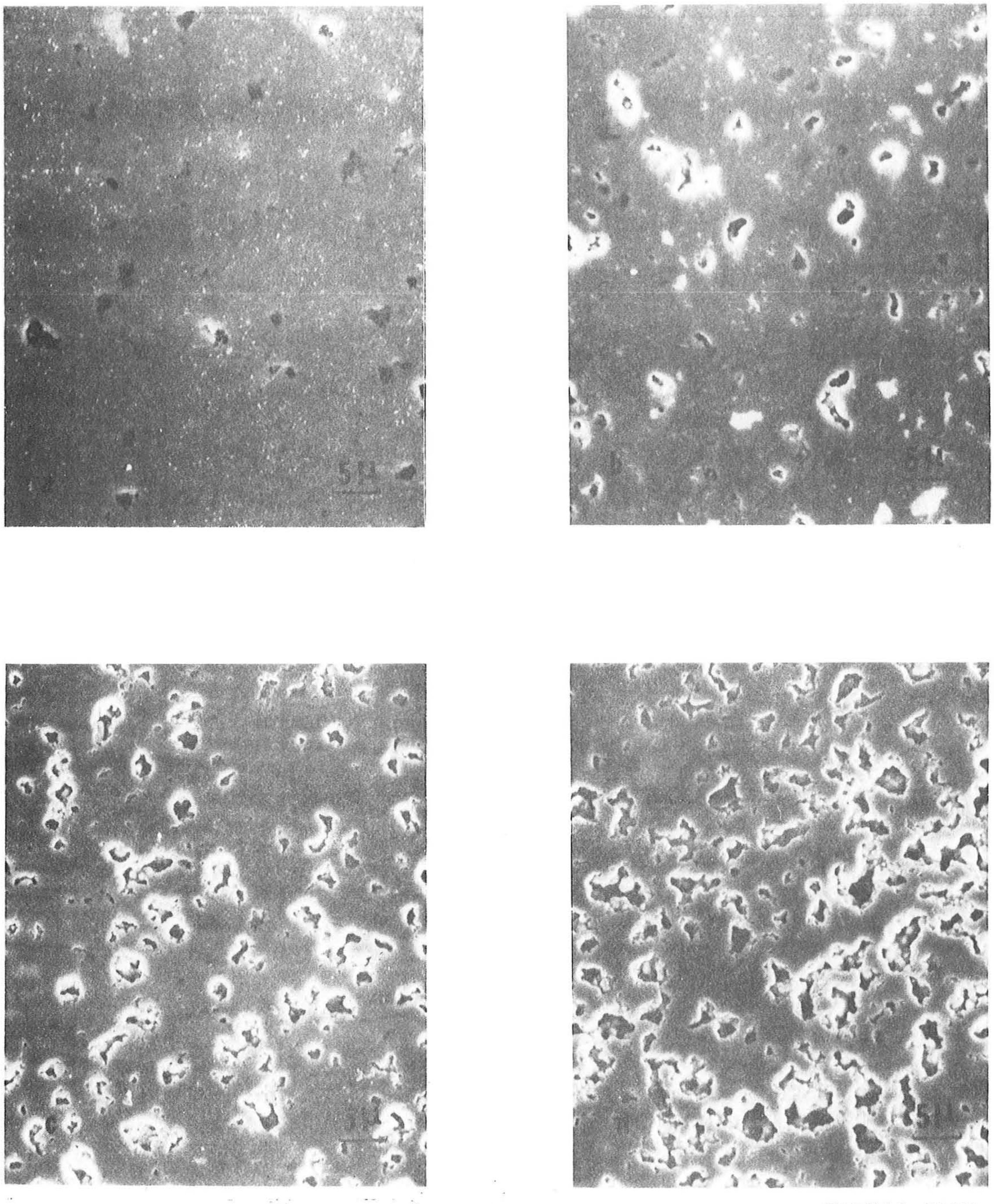

XBB766-5227

Fig. 14. Random sections of PNZT-fine pore specimens showing the size and distribution of the porosity; (a) 2.40%, (b) 5.16%, (c) 7.50%, and (d) 16.40% porosity.

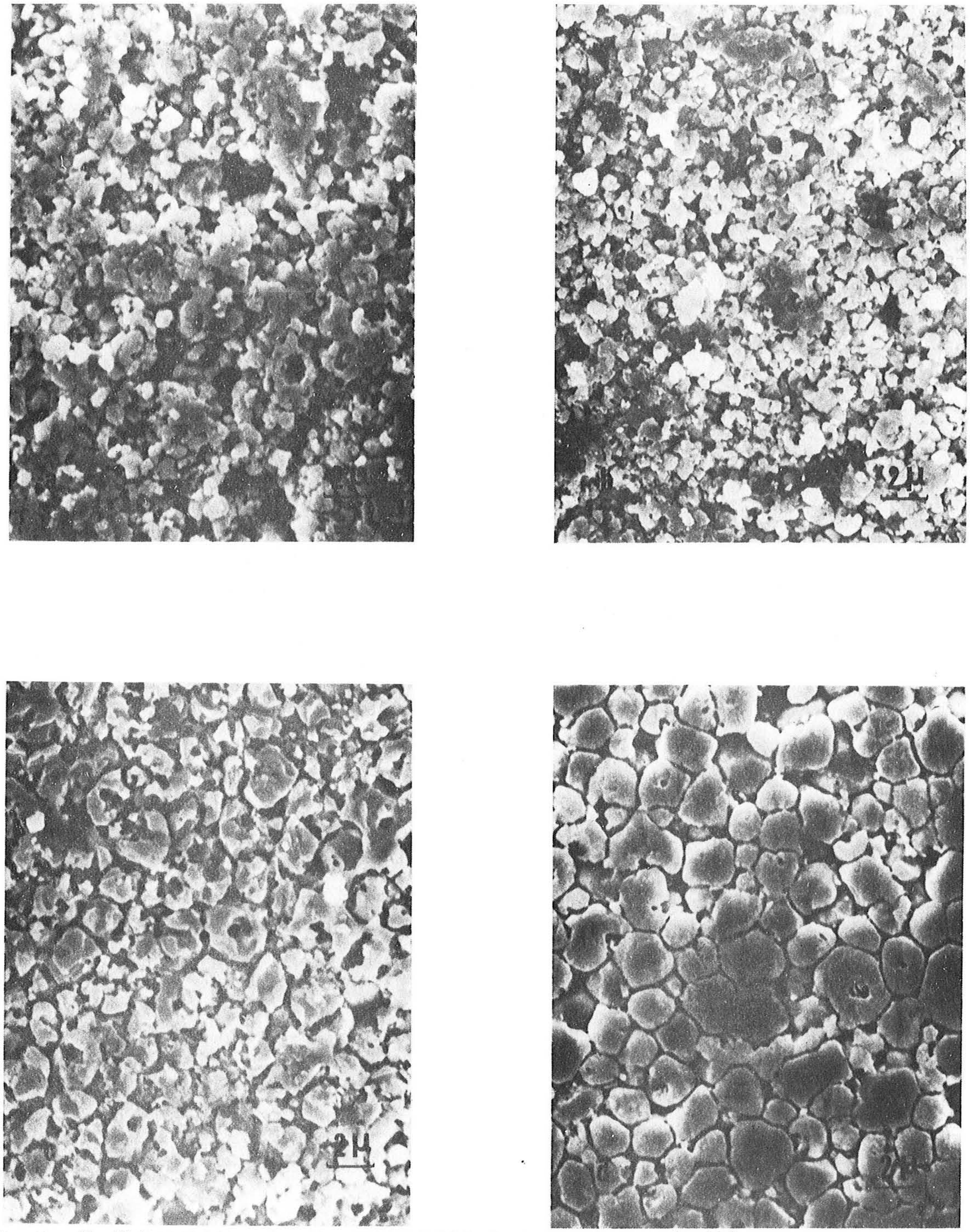

XBB766-5230

Fig. 15. Microstructures of PNZT-fine pore specimens from varying sintering conditions (sintering temperature, cold pressing pressure and sintering time); (a) 5.16 % porosity, 1150°C, 1 ton pressing pressure, 1 minute, (b) 2.40% porosity, 1150°C, 4 ton pressing pressure, 1 minute, (c) 1.20% porosity, 1150°C, 4 ton pressing pressure and one hour holding time at temperature, and (d) near theoretical density, 1200°C, 4 ton pressing pressure and 16 hours holding time at temperature.

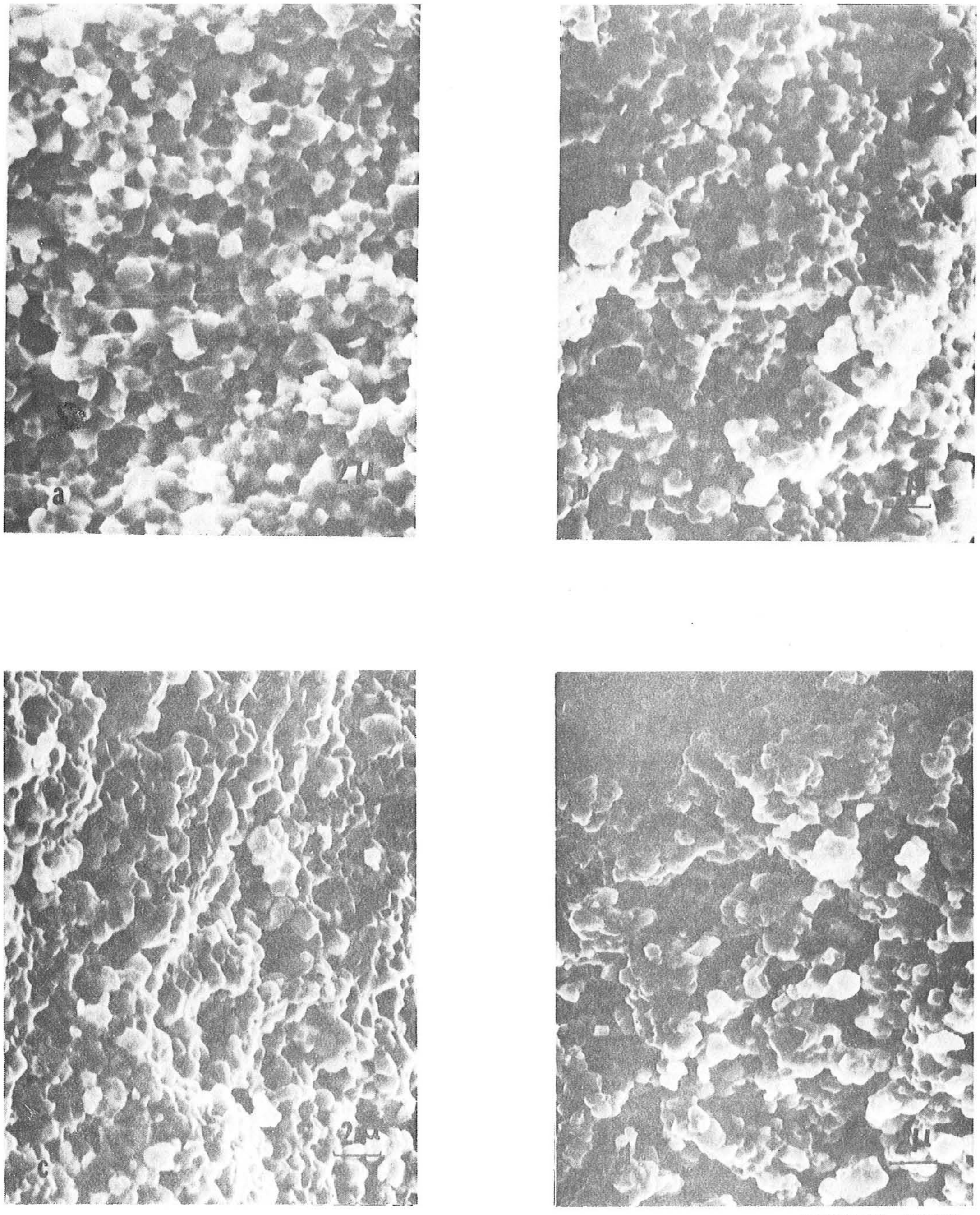

XBB766-5228

Fig. 16. Fracture surfaces of PNZT-fine pore specimens showing mostly intergranular fracture. (a) 2.40% porosity, (b) 7.50% porosity, (c) 5.16% porosity, and (d) 16.40% porosity.

Table IV. Compilation of Pore Size and Grain Size of PNZT Ceramics

Starting Powder	System	Volume Percent Porosity	Pore Size µm	Grain Size µm
PNZT + 5 w/o excess PbO	PNZT			2-5
PNZT + 5 w/o excess PbO	PNZT + Spherical Pores	Up to 13.5%	25-40 60-75 110-150	2-5 2-5 2-5
	PNZT + Acicular Pores	Up to 11.4%	45-60 110-150	2-5 2-5
	PNZT + Fine Pores	1.20 2.40 5.16 7.50 13.63 15.33 16.40	<2 2 2 2 2 2 2	1-5 <3 <3 <3 <3 <3 <3
PNZT + 1 w/o excess PbO	PNZT + Spherical Pore	2.45 4.90	110-150 110-150	2-8 2-8
	PNZT + Fine Pore	4.80	2-3	<3

surfaces of PNZT and PNZT - porous specimens are shown in Fig. 17 and 18. Mostly intergrannular fracture (Fig. 16) was observed, however, in a few cases a combination of intergrannular and transgrannular fracture was observed at high magnifications. Fracture may initiate from either the tensile surface, the edges of the specimen, or just beneath the tensile surface.

Although the tensile stress is maximum at the outer fiber of the specimen in a bend test, a pore or agglomeration of pores can cause high stress concentrations below the surface which can initiate fracture. This is clearly observed in Fig. 18 where small pores are probably linked up to a long narrow flaw that raised the stress to a critical value and caused failure.

Calculation of the critical flaw size, "a", can be done from the Griffith-Irwin relationship as, $a = f\left(\frac{Z}{Y}\right)\left(\frac{K_{IC}}{\sigma}\right)^2$ → (27) where Z is the flaw shape parameter, Y is a geometrical parameter,[21,28] K_{IC} is the fracture toughness and σ is the fracture strength of the material. For the same volume percent porosity (say 4.8%), when K_{IC} values are taken from Table VIII and σ values from Fig. 10, it is found that the critical flaw size for the PNZT - large pore system is about one and a half times larger than for the PNZT - fine pore system [assuming $f\left(\frac{Z}{Y}\right)$ is same for both cases]. Thus the strength of PNZT - fine pore specimen [for 4.8% porosity] should be expected to be about 1.25 times higher [as $\sigma \propto \frac{1}{\sqrt{a}}$] than for the PNZT - large pore specimen at the same volume percent porosity and this is shown in Fig. 11.

It was observed that sometimes the bend specimens failed from the edges. To determine the edge effect[29] on the fracture strength, specimens were

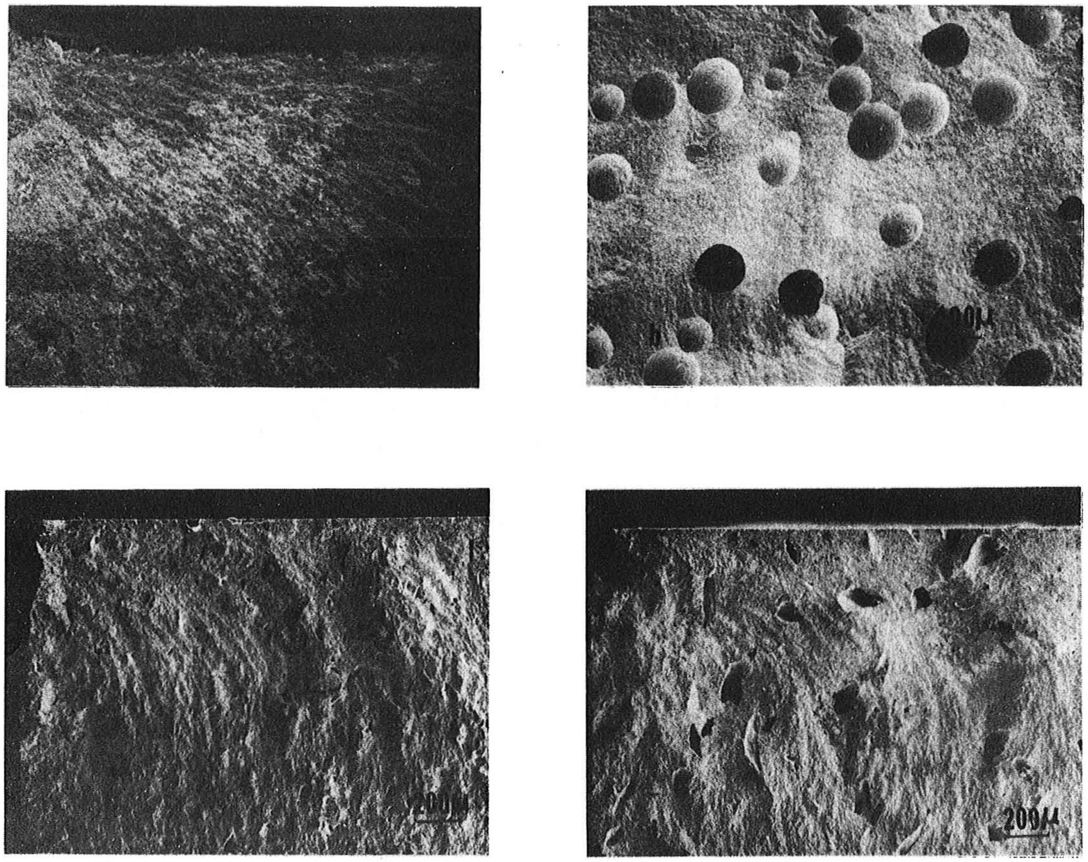

XBB766-5231

Fig. 17. Typical fracture surfaces of PNZT specimens. (a)* dense PNZT ceramic with a river pattern from the edge of the specimen, (b)* PNZT-spherical pore (8.95%, 110-150μm), (c) PNZT-acicular pore (3.55%, 45-60μm), river pattern and initiation of edge failure, and (d) PNZT-acicular pore (4.66%, 110-150μm) with an indication of edge failure.

*Courtesy of Dr. R. W. Rice, Naval Research Lab., Washington, DC.

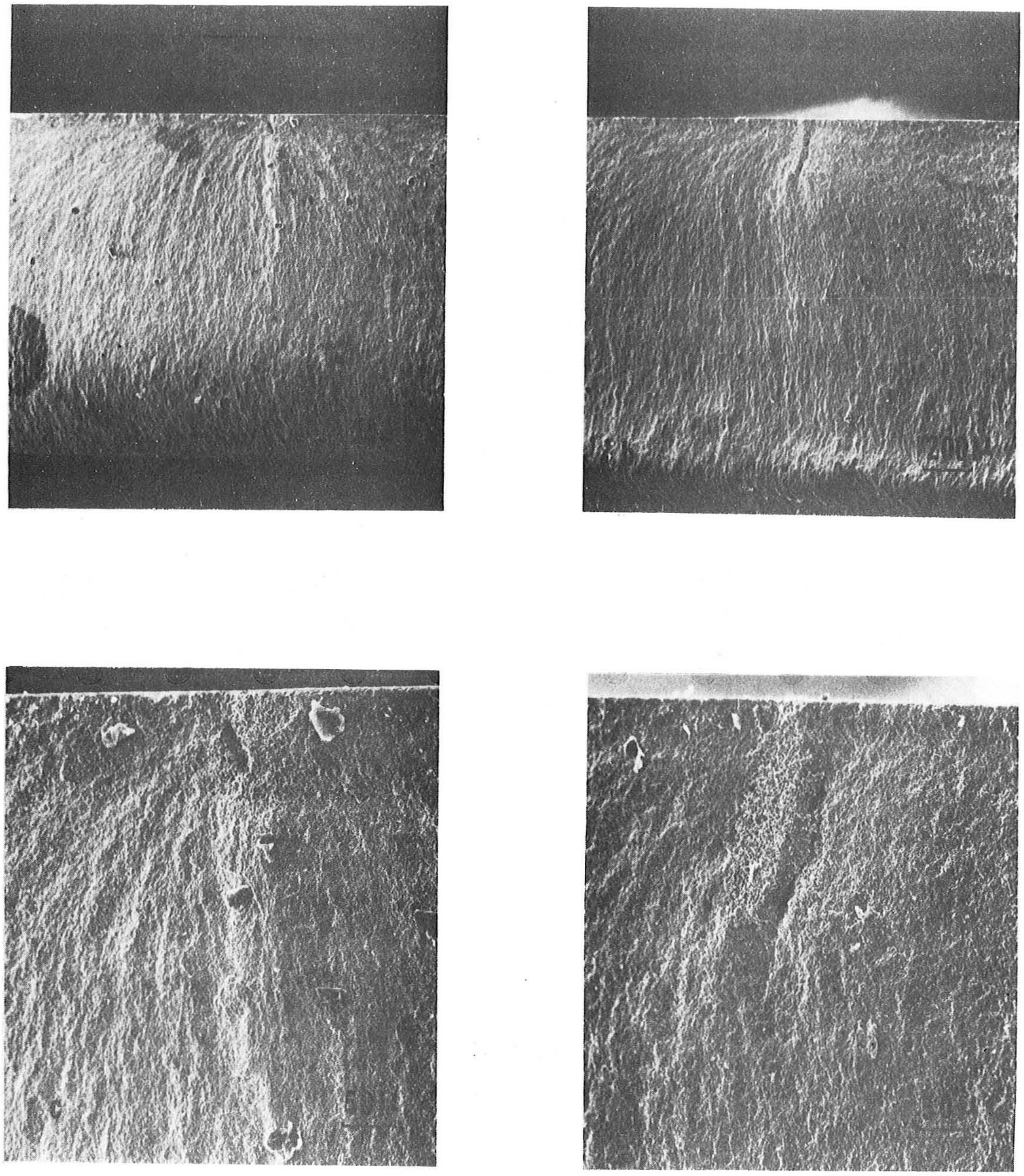

XBB766-5229

Fig. 18. Fracture origin for PNZT-fine pore specimens (a and c) 2.40% porosity and (b and d) 5.16% porosity at two different magnifications. Note that the river pattern and the fracture origin at an agglomeration of pores underneath the tensile surface.

fabricated by the same processing techniques. The PNZT pellets were cut into thin slices for fracture strength measurement. In one third of the specimens, the edges were carefully rounded by using a rotating diamond wheel. For the other third of the specimens, after rounding the edges, the tensile surface was polished, and the final one third of the specimens were tested as cut. The results are shown in Table V. It was found that the change in fracture strength was insignificant. The fracture surfaces are shown in Fig. 19 for an edge rounded specimen and an edge rounded and polished specimen. In both cases the fracture originates somewhere along the width rather than the edges of the specimens. Figures 19 a and 19 c show that fracture initiates from the tensile surface where grain boundary cracks are probably generated from the machining. In Fig. 19 b and 19 d, the surface was polished and the fracture originates beneath the polished tensile surface, probably the surface stress is raised by subsurface flaws.

C. Elastic Modulus and Damping Capacity

The modulus is a measure of the strength of the bonding among atoms in the lattice and it is the slope of the linear elastic region of the stress-strain curve. Elastic modulus, E, of PNZT ceramics was measured by a sonic resonance technique. The values of E are given in Table VI and the results are plotted in Fig. 20. The elastic modulus follows a straight line relationship with porosity. The linear relationship of the form

$$E/E_o = 1-KP \tag{19}$$

describes the experimental results. The value of K is found to be 2.5 for PNZT ceramics. The elastic modulus extrapolated to zero porosity at

Table V. Fracture Strength of PNZT Ceramics

Surface Conditions	Mean Fracture Strength, σ_{mean} PSI
As cut surface.	12,320 ± 7.2%
As cut surface and rounding off the edges.	12,780 ± 7.3%
Polished Surface and rounding off the edges.	12,370 ± 8.0%

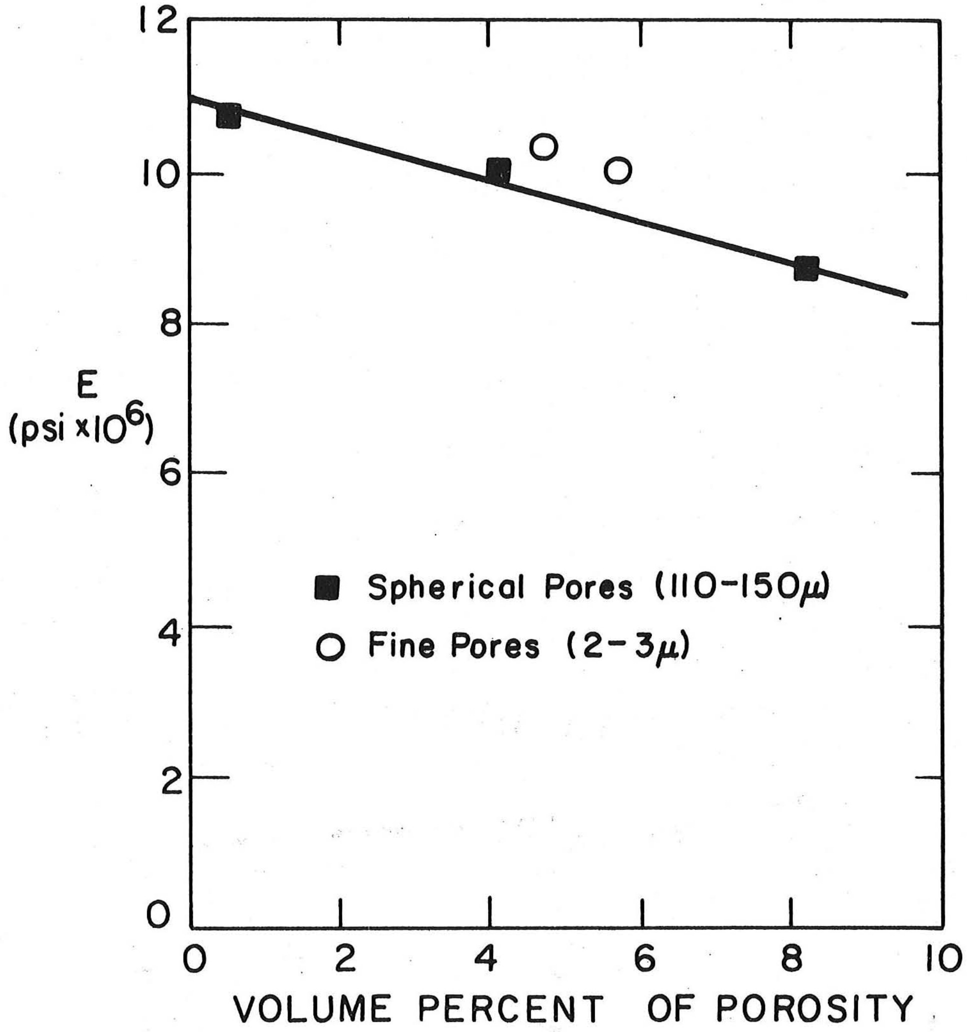

XBL 766-7028

Fig. 20. Elastic modulus of PNZT ceramics is plotted against the volume percent of porosity.

room temperature is 11.0 x 10^6 psi. For fine pores (2-3μm) the elastic modulus shows a slightly higher value compared to PNZT ceramic containing the same volume percent of porosity but large in size (110-150μm).

Damping is determined by observing the decay in amplitude of vibration during free oscillation after energy fed into the test specimen is interrupted. The natural frequency used to calculate the elastic modulus is theoretically correct only for the materials without internal damping. In the present case, damping capacity, δ, was calculated from Equation (25), and the results are given in Table VII. Damping capacity is plotted against volume percent of porosity in Fig. 21. It was found that with increase in porosity, the damping capacity increases. An interesting observation in Fig. 21 is that for PNZT specimens containing fine pores (2-3μm) generated by low temperature (1150°C), short time firing, the damping capacity is approximately one third that for large pore specimens. It is even less than the extrapolated damping capacity value for porosity free specimens. For PNZT- fine pore specimens (sintered at low temperature) it has been mentioned that the grain boundary structure may be different because of the presence of a small amount of PbO from the residual liquid phase. This will probably make the PNZT matrix more continuous. The dissipation of energy will be less for PNZT-fine pore specimens and reflected in low damping capacity.

D. Fracture Toughness

Measurement of fracture toughness provides an empirical measure of the effect of microstructure on crack propagation. Using the double torsion technique, the fracture toughness K_{IC} was measured for PNZT ceramics. A considerable amount of difficulty arose in fabricating the

Table VII. Damping Capacity of PNZT Ceramics

Type of pores	Volume Percent Porosity	Pore Size μm	Damping Capacity δ
Spherical	0.55	110-150	0.0175
	4.07		0.0273
	8.27		0.0449
Fine	4.70	2-3	0.0079
	5.70		0.0150

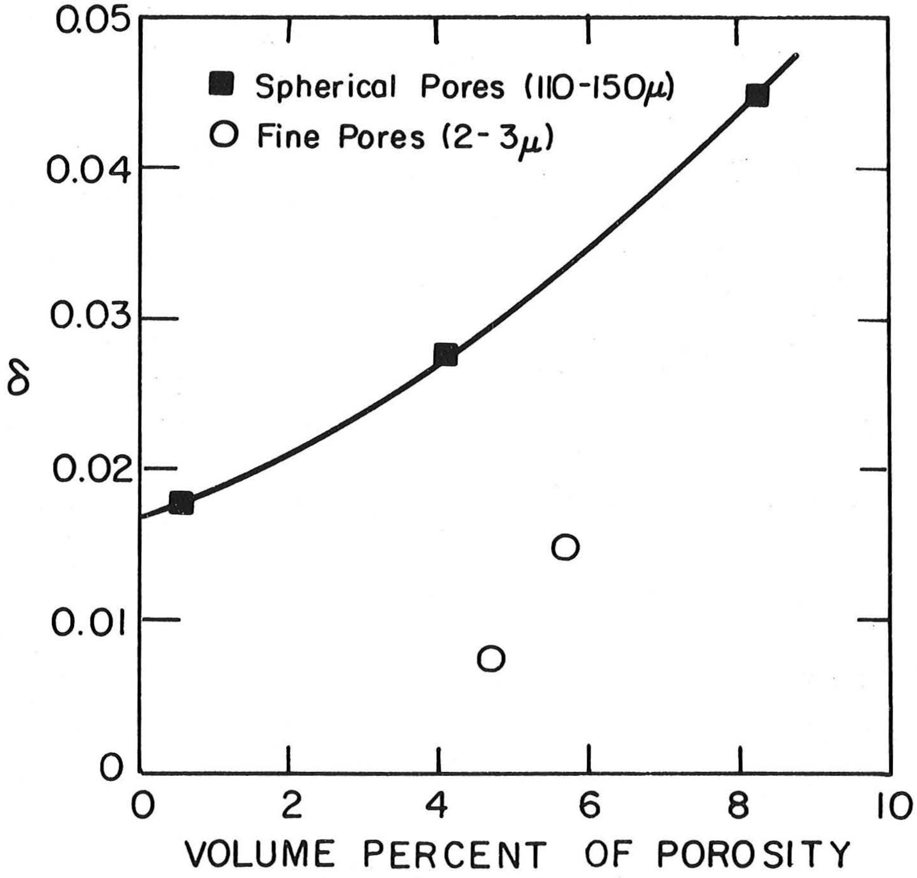

XBL 766-7027

Fig. 21. Damping capacity as a function of volume percent of porosity.

ceramic by sintering a large piece from which the double torsion specimens were cut. 5 w/o excess PbO (P-1 Powder) caused large cracks to form in the interior of the piece. This was completely eliminated by reducing the amount of excess PbO to 1 w/o (P-2 Powder). For comparison purposes, two pellets [using P-1 and P-2 Powders] were sintered and their fracture strength was measured by 4-point bending. It was found that the strengths were almost identical.

Double torsion specimens were also tested in a 4-point bending machine using point loading[30] instead of the knife edge supports used for fracture strength measurement. The results of K_{IC} are given in Table VIII and a plot of K_{IC} vs. volume percent porosity is shown in Fig. 22. K_{IC} decreases with increasing porosity (110-150μm) and shows a slightly higher value for fine pores (2-3μm) specimens. Also in Table VIII, the values of G_{IC} and γ_F calculated from Equation(21),are given. G_{IC} also decreases with increase in porosity but the rate of decrease is less compared to K_{IC} as E also decreases with increase in porosity.

The expression for K_I for the double torsion specimen geometry shows[24] that K_I is not a function of crack length but it is directly dependent on the applied load at the point of fracture. PNZT - fine pore specimen fractures at a higher stress than PNZT - large pore specimen as observed and explained earlier. Therefore, for PNZT - fine pore materials, the load at the point of fracture is higher. This leads to a higher K_{IC} value for PNZT ceramics containing fine pores (2-3μm) compared to PNZT - spherical pore (110-150μm) system. K_{IC} is related to G_{IC} according to Equation(21)and, therefore, G_{IC} follows a similar trend as that of K_{IC}. The microstructures of PNZT ceramic with 1 w/o excess

Table VIII. Fracture Mechanics Parameters for PNZT Ceramics

Volume Percent Porosity	Pore Size µm	K_{IC} PSI-in$^{1/2}$	E PSIx10^{6}	G_{IC} PSI-in	γ_F $\frac{\text{ergs}}{\text{cm}^2} \times 10^4$
-	-	1470 ± 4.2%	11.00	0.179	1.570
2.45	110-150	1344 ± 4.3%	10.30	0.160	1.402
4.90	110-150	1277 ± 5.8%	9.65	0.154	1.354
4.80	2-3	1388 ± 15.2%	~10.3	0.171	1.498

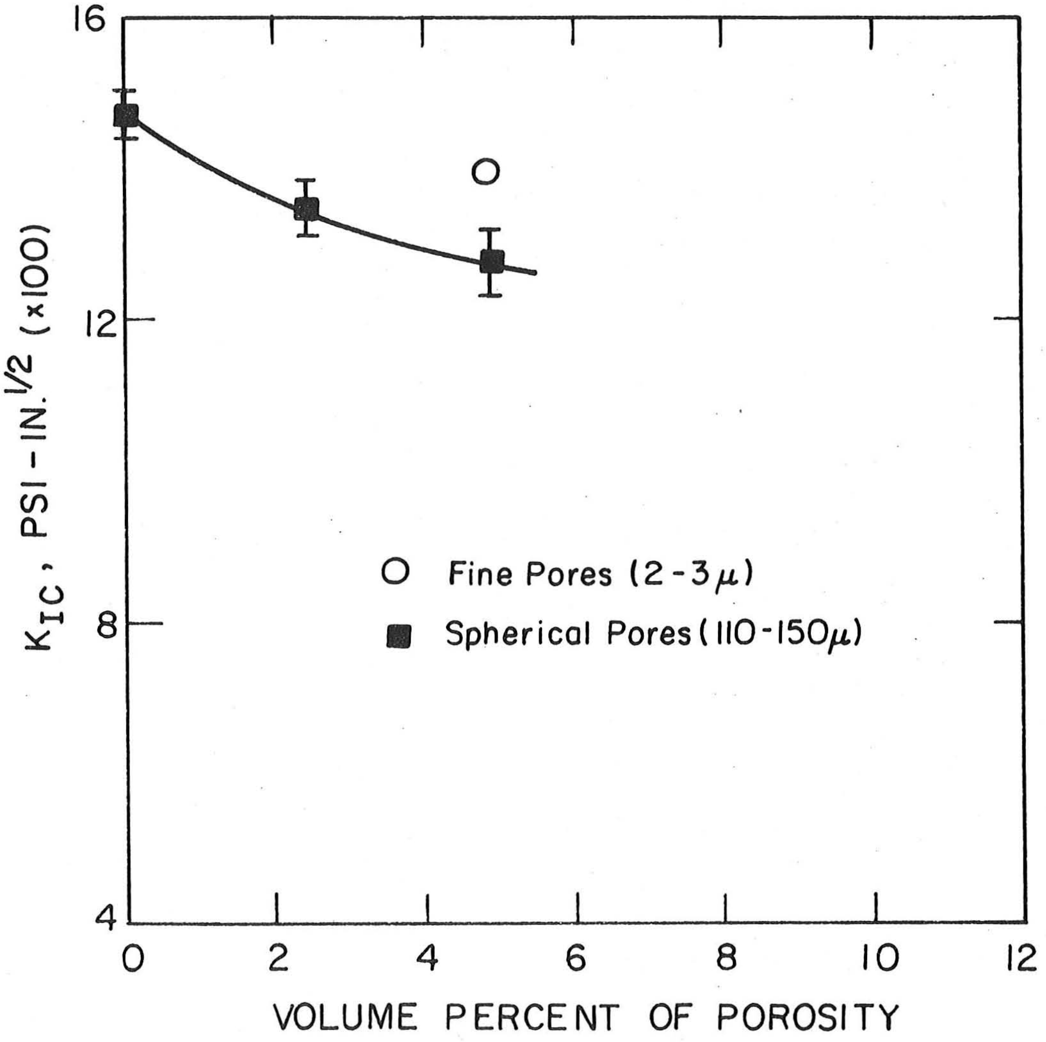

XBL 766-7044

Fig. 22. Fracture toughness values are plotted against the volume percent of porosity.

PbO to start with, containing spherical and fine pores are shown in Fig. 23. Grain size in the dense PNZT matrix for the large pore specimen is between 2 to 8μm and pore size and grain size (around 3μm) are almost identical for PNZT- fine pore materials. For artificially introduced large pores, a pore was observed at the crack front and shown in Fig. 24.

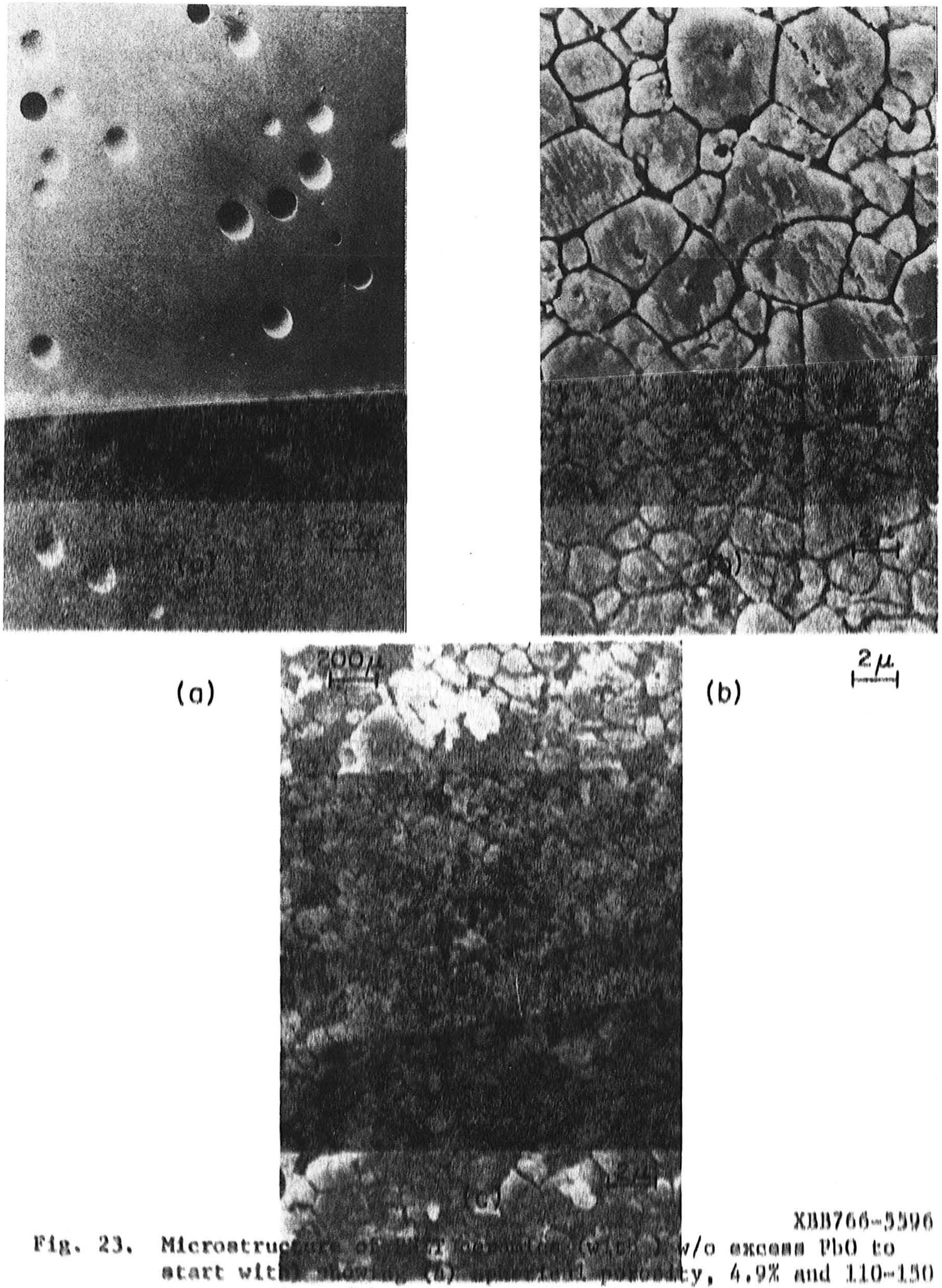

XBB766-5596

Fig. 23. Microstructure of PNZT ceramics (with 1 w/o excess PbO to start with) showing (a) spherical porosity, 4.9% and 110-150 μm pore size, (b) grain size distribution in nearly theoretical dense specimen, and (c) grain and pore distributions in PNZT-fine pore (4.8%) specimen.

XBB766-5596

Fig. 23. Microstructure of PNZT ceramics (with 1 w/o excess PbO to start with) showing (a) spherical porosity, 4.9% and 110-150 μm pore size, (b) grain size distribution in nearly theoretical dense specimen, and (c) grain and pore distributions in

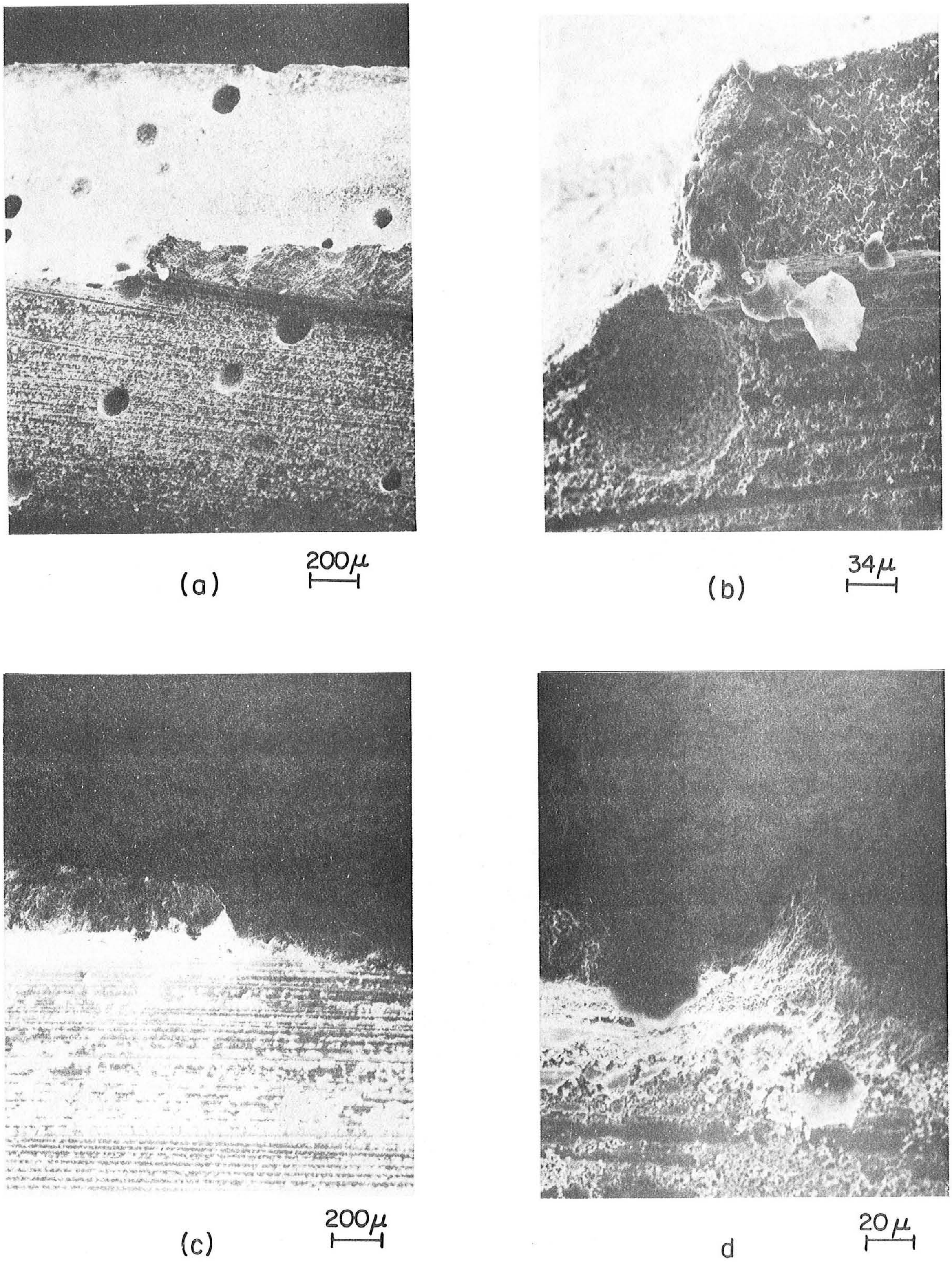

XBB766-5595

Fig. 24. Fractured surfaces from specimens after double torsion testing, (a and b) 4.9% porosity, 110-150 μm, (c and d) 4.8% fine porosity, at two different magnifications. Note a large spherical pore at the crack front in the top right micrograph.

VI. SUMMARY AND CONCLUSION

Porous ceramics with spherical or acicular pores (25-150μm diameter) were fabricated by admixing organic powders. The matrix grain size of these samples was kept constant (2-5μm). Very fine pores (2-3μm diameter) were formed in PNZT ceramics by varying the sintering conditions. In this case, the grain size was comparable to the pore size.

The effect of porosity on the fracture strength of spherical and acicular pore systems followed quite well the Weibull's statistical approach. Other approaches which might be considered based on the stress concentration factor or effective cross-sectional area were inadequate to explain the experimental data. An interesting feature of Weibull's analysis is the prediction that only the total porosity and not the pore size will control the strength when the pore diameter is much larger than the grain size. When the pore size is comparable to the grain size (PNZT-fine pore), Weibull's predictions is not followed. The experimental results of increasing porosity to 5% follow the results expected from a simple model of decreasing cross-sectional area with increasing porosity. The critical flaw size for PNZT- fine pore specimen is smaller than PNZT- large pore specimen and that gives a higher strength for fine pore specimen.

The elastic modulus of PNZT ceramics shows a linear decrease with increase in porosity (110-150μm diameter). Fine pore materials at the same volume percent porosity show a slightly higher modulus. Damping capacity increases with increase in porosity (110-150μm diameter). For specimens with small pores on the order of the grain size the damping was approximately one third that of large pore systems. Low damping is probably due to the presence of small amounts of residual PbO in the grain boundaries.

Fracture toughness, K_{IC} of PNZT ceramics shows a decrease with increase in porosity (110-150μm) - so does the critical strain energy release rate, G_{IC}, and fracture surface energy, γ_F. K_{IC}, G_{IC} and γ_F for PNZT- fine pore (2-3μm) system shows a higher value at the same volume percent porosity.

For polycrystalline lead zirconate-titanate ceramics doped with niobium, small pores give a higher strength, elastic modulus, fracture toughness and fracture surface energy compared to ceramics with the same volume percent of large pores.

ACKNOWLEDGMENT

I would like to express my deep appreciation to Professor Richard M. Fulrath for his guidance throughout the course of this work. Additional appreciation is expressed to Professor Iain Finnie for his helpful suggestions and comments, and to Professor Joseph A. Pask for his comments and editing the thesis. Discussions with Ö. Vardar, David Wang and Vimal Pujari and other friends were useful and are also acknowledged. Thanks are extended to Gloria Pelatowski for drafting and Gay Brazil for typing the dissertation.

Finally I would like to thank my parents Mr. and Mrs. Debendra Nath Biswas and to my entire family members for their continuous encouragement at all times.

This work was carried out under the auspices of the Energy Research and Development Administration.

REFERENCES

1. M. Y. Bal'shin, Powder Metallography (in Russian), Metallurgizdat, Moscow (1948).
2. E. Ryshkewitch, "Compression Strength of Porous Sintered Alumina and Zirconia," J. Am. Ceram. Soc., 36 [2], 65-68 (1953).
3. W. Duckworth, "Discussion of Ryshkewitch Paper," Ibid., P. 68.
4. R. L. Coble and W. D. Kingery, "Effect of Porosity on Physical Properties of Sintered Alumina," Ibid., 39(11) 377-85 (1956).
5. F. P. Knudsen, "Dependence of Mechanical Strength of Brittle Polycrystalline Specimens on Porosity and Grain Size," Ibid., 42(8) 367-87 (1959).
6. E. M. Passmore, R. M. Spriggs and T. Vasilos, "Strength-Grain Size - Porosity Relations in Alumina," Ibid., 48(1) 1-7 (1965).
7. J. E. Bailey and N. A. Hill, "The Effect of Porosity and Microstructure on the Mechanical Properties of Ceramics," Proc. Brit. Ceram. Soc., No. 15, P. 15-35 (1970).
8. S. C. Carniglia, "Working Model for Porosity Effects on the Uniaxial Strength of Ceramics," J. Am. Ceram. Soc., 55(12) 610-18 (1972).
9. W. Weibull, Ingvetenskakad, Handl. No. 151, Stockholm (1939).
10. Ö. Vardar and I. Finnie, "An Analysis of the Brazilian Disk Fracture Test Using the Weibull Probabilistic Treatment of Brittle Strength," Int. J. of Fracture, Vol. 11, No. 3, P. 495-508 (1975).
11. I. Finnie and Ö. Vardar, Dept. of Mech. Eng., U.C. Berkeley, California. Private communication.
12. J. N. Goodier, "Concentration of Stress Around Spherical and Cylindrical Inclusions and Flaws," J. Appl. Mech. 1(1) 39-44 (1933).

13. J. K. MacKenzie, "Elastic Constants of a Solid Containing Spherical Holes," Proc. Phy. Soc. (London), 63B(1), 2-11, (1950).

14. Z. Hashin, "Elastic Moduli of Heterogeneous Materials," J. Appl. Mech., 29(1) 143-50 (1962).

15. D. P. H. Hasselman, "Porosity Dependence of the Elastic Moduli of Polycrystalline Refractory Materials," J. Am. Ceram. Soc., 45 (9) 452-53 (1962).

16. R. M. Spriggs, "Expression for Effect of Porosity on Elastic Modulus of Polycrystalline Refractory Materials, Particularly Aluminum Oxide," Ibid., 44(12) 628-29 (1961).

17. F. P. Knudsen, "Effect of Porosity on Young's Modulus of Alumina," Ibid., 45(2) 94-95 (1962).

18. D. P. H. Hasselman and R. M. Fulrath, "Effect of Small Fraction of Spherical Porosity on Elastic Moduli of Glass," Ibid., 47(1) 52-53 (1964).

19. P. C. Paris and G. C. Sih, "Stress Analysis of Cracks", ASTM Special Tech. Publ. No. 381 (1965).

20. A. G. Evans, "Fracture Mechanics of Ceramics," Ed. by R. C. Bradt, D. P. H. Hasselman and F. F. Lange, Plenum Press, NY-London, Vol. 1 17-48 (1974).

21. W. F. Brown and J. E. Srawley, "Plane Strain Crack Toughness Testing of High-Strength Metallic Materials," ASTM Special Tech. Publ. No. 410, 1-15, (1967).

22. D. R. Biswas and R. M. Fulrath, "Strength and Fracture in Glass Matrix Composites," J. Am. Ceram. Soc., 58 (11-12), 526-27 (1975).

23. D. P. H. Hasselman, "Tables for the Computation of Shear Modulus and Young's Modulus of Elasticity from the Resonant Frequency of Rectangular Prisms," Applied Research Branch, Research and Development Div., The Carborundum Co., Niagara Falls, New York, (1961).

24. D. P. Williams and A. G. Evans, "A Simple Method for Studying Slow Crack Growth," J. Test. Eval., 1(4) 264-70 (1973).

25. O. Vardar, I. Finnie, D. R. Biswas and R. M. Fulrath, "Effect of Spherical Pores on the Strength of Polycrystalline Ceramic," Submitted to Int. J. of Fracture, (LBL-4575), Dec. (1975).

26. R. Jaffee, W. R. Cooke, Jr., and H. Jaffee, "Piezoelectric Ceramics," Academic Press, London-New York, P. 16 (1971).

27. A. G. Evans and G. Tappin, "Effect of Microstructure on the Stress to Propagate Inherent Flaws," Proc. Brit. Ceram. Soc., 20, 275-97 (1972).

28. G. K. Bansal, "Effect of Flaw Shape on Strength of Ceramics," J. Am. Ceram. Soc., 59, 1-2, 87-88 (1976).

29. R. W. Rice, Naval Research Laboratory, Washington, DC, Private communication.

30. A. G. Evans, Rockwell International Science Center, Thousand Oaks, California, Private communication.